Probing quantum spin liquids with a quantum twisting microscope

Valerio Peri [1,*], Shahal Ilani [2], Patrick A. Lee [3], and Gil Refael[1]

[1]*Department of Physics, IQIM, California Institute of Technology, Pasadena, California 91125, USA*
[2]*Department of Condensed Matter Physics, Weizmann Institute of Science, Rehovot 76100, Israel*
[3]*Department of Physics, Massachusetts Institute of Technology, Cambridge, Massachusetts 02139, USA*

The experimental characterization of quantum spin liquids poses significant challenges due to the absence of long-range magnetic order, even at absolute zero temperature. The identification of these states of matter often relies on the analysis of their excitations. In this paper, we propose a method for detecting the signatures of the fractionalized excitations in quantum spin liquids using a tunneling spectroscopy setup. Inspired by the recent development of the quantum twisting microscope, we consider a planar tunneling junction, in which a candidate quantum spin-liquid material is placed between two graphene layers. By tuning the relative twist angle and voltage bias between the leads, we can extract the dynamical spin structure factor of the tunneling barrier with momentum and energy resolution. Our proposal presents a promising tool for experimentally characterizing quantum spin liquids in two-dimensional materials.

I. INTRODUCTION

Quantum spin liquids (QSLs) are states of matter that defy magnetic ordering even at temperatures far below their exchange energy. While theoretical understanding of QSLs has made significant progress [1–3], experimental verification of these states of matter remains a formidable challenge [4–6]. The absence of order serves as an imperfect definition, as it is impossible to rule out all possible ordered states. A more experimentally accessible characteristic of QSLs is the presence of emergent gauge field and low-energy excitations with fractionalized quantum numbers, such as spinons, which carry fractional spin and zero charge.

Several experimental techniques have been employed to investigate the signatures of fractionalized excitations in potential QSL materials. Thermal transport measurements, for instance, have been used to explore the low-energy physics of α-RuCl$_3$ [7], volborthites [8], κ-(ET)$_2$Cu$_2$(CN)$_3$ [9], and organic dmits [10]. Optical absorption and Raman spectroscopy have provided access to the zero-momentum excitation spectrum of pyrochlores [11], herbertsmithite [12], and Kitaev materials [13–16]. Nuclear magnetic resonance and muon spin relaxation have enabled to locally probe these candidate materials [17,18]. Additionally, spin transport [19,20], NV centers [21–23], and numerous other techniques [24–29] have been proposed for investigating QSLs. Inelastic neutron scattering [30–35], however, stands out due to its unique advantage of probing the excitation spectrum with both momentum and energy resolution. Unfortunately, a major limitation of inelastic neutron scattering is its reliance on large bulk three-dimensional crystals. This drawback renders it unsuitable for studying QSLs in the monolayer and few-layer limit, which attracted considerable interest with the emergence of high-quality two-dimensional materials [36].

Inspired by the recent development of the quantum twisting microscope [37], we consider a planar junction formed by two graphene layers separated by a QSL material, depicted in Fig. 1(a), as a technique for investigating the fractionalized excitations in two-dimensional materials. Traditional tunneling probes offer limited momentum resolution, thereby restricting their capability to fully characterize these excitations [38–54]. In our proposal, the momentum resolution is achieved by controlling the relative twist angle θ between the graphene layers. A finite twist angle introduces a momentum mismatch $\Delta \boldsymbol{K}$ between the Dirac cones of the two graphene layers. In the absence of the QSL barrier, as depicted in Fig. 1(b), the direct tunneling of electrons can occur if $\hbar v_F |\Delta \boldsymbol{K}| < eV_{tb} + 2\mu$, where eV_{tb} is the voltage bias between the layers and μ the chemical potential [37,55–57]. If we continue increasing the twist angle while keeping the voltage bias fixed, the direct tunneling gets suppressed. When the tunneling barrier hosts low-energy excitations, however, additional processes come into play. The graphene's electrons can change their energy and momentum by scattering from the excitations in the QSL. Consequently, these additional inelastic processes contribute to the total current even when $\hbar v_F |\Delta \boldsymbol{K}| > eV_{tb} + 2\mu$ [38–40] [see Fig. 1(c)]. This inelastic contribution to the tunneling current offers valuable insights into the excitation spectrum and the underlying dynamics of the QSL.

The central result of our study is captured by Eq. (18). By considering the second derivative of the tunneling current with respect to the voltage bias, i.e., the inelastic electron tunneling spectroscopy (IETS) signal, we access the dynamical spin structure factor of the tunneling barrier at momentum $\Delta \boldsymbol{K}$ and energy eV_{tb}. The twist angle determines the separation between the Dirac cones of the two graphene layers and controlling it provides the sought-after momentum resolution.
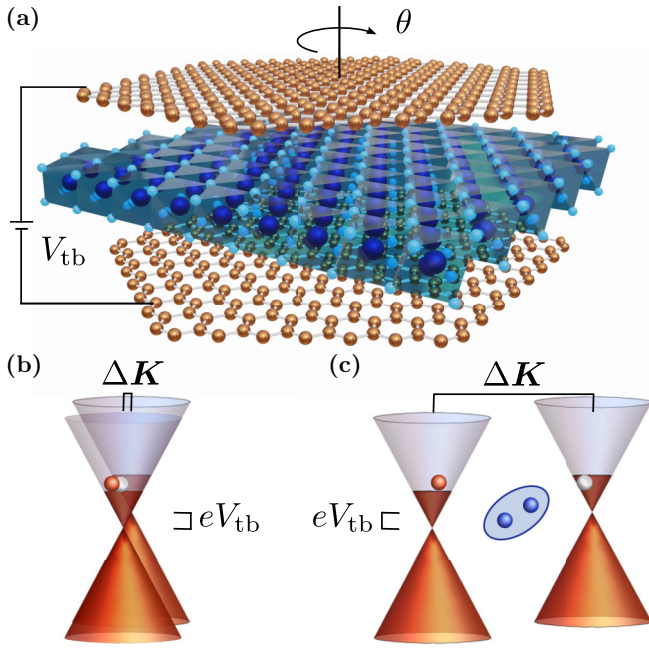
*vperi@caltech.edu

FIG. 1. (a) Schematic representation of the tunneling heterostructure. The top and bottom layers are graphene, while the middle barrier is a monolayer of a candidate QSL material, e.g., 1T-TaS$_2$. V_{tb} is the voltage bias between the graphene layers, while θ is the relative twist angle between them. Two distinct tunneling processes can take place. (b) Direct tunneling can occur only if $\hbar v_F |\Delta K| < eV_{tb} + 2\mu$ such that the momentum and energy of the graphene's electron are conserved. The tunneling process corresponds to a particle-hole excitation across the layers. (c) The low-energy excitation of the barrier can mediate additional inelastic tunneling processes through which the graphene's electron changes its momentum and energy. The electron can then tunnel even when the Dirac cones of the two layers are further apart compared to (b), i.e., $\hbar v_F |\Delta K| > eV_{tb} + 2\mu$. An example of a QSL excitation, i.e., a spinon particle-hole excitation, is here schematically represented in blue.

This additional tunable knob enables qualitative and quantitative distinction among various QSLs, facilitating the inference of the microscopic Hamiltonian governing a candidate QSL material.

The development of probes capable of providing momentum and energy resolution similar to inelastic neutron scattering but tailored for two-dimensional materials is highly desirable. This is particularly important considering the potential existence of materials that exhibit QSL behavior exclusively in the monolayer limit. One intriguing example is 1T-TaS$_2$, a layered transition metal dichalcogenide (TMD). Below a critical temperature of approximately 200 K, it undergoes a commensurate $\sqrt{13} \times \sqrt{13}$ charge-density wave (CDW) transition. The CDW arrangement forms a triangular lattice of stars of David, each containing an odd number of electrons per unit cell. The residual Coulomb interaction in this system induces a Mott-insulating gap of 400 meV [58,59]. Interestingly, no magnetic ordering has been observed down to very low temperatures, leading to suggestions that it may host a gapless QSL [60–64]. However, in the bulk material, the formation of interlayer dimers can compete with the Mott

physics picture, potentially opening a trivial band-insulator gap [65–69]. Nevertheless, the possibility of observing a QSL in a monolayer of 1T-TaS$_2$ remains promising.

In this work, our primary focus is on QSLs, which are intriguing and elusive states of matter that demand new experimental probes. Nonetheless, our proposal equally applies to the study of arbitrary magnetic barriers. For instance, it can be used to investigate magnon excitations in magnetically ordered materials [40,41,52]. Therefore, we anticipate that the quantum twisting microscope [37] will expand our understanding of magnetic interactions in two-dimensional materials.

The remainder of the paper is organized as follows. In Sec. II, we introduce the setup, describing the tunneling through a QSL in a quantum twisting microscope. In Sec. III, we demonstrate how, under a set of simplifying assumptions, the inelastic electron tunneling spectroscopy signal contains a contribution directly proportional to the dynamical spin structure factor of the QSL. Section IV focuses on studying the spin structure factor of different types of QSLs via a mean-field approximation and showcases how our proposal can distinguish among them. Finally, we provide concluding remarks in Sec. V.

II. TUNNELING THROUGH A QUANTUM SPIN LIQUID IN A QUANTUM TWISTING MICROSCOPE

We investigate the vertical tunneling of electrons between two twisted graphene layers, separated by a QSL material that acts as a tunneling barrier. The twist angle between the graphene layers, denoted by θ, can be controlled *in situ*, and a voltage bias, denoted by V_{tb}, is applied across them. While a similar setup has been explored in Ref. [42], the tunability of the twist angle was not considered. The recent development of the quantum twisting microscope [37] motivates us to investigate the potential of this additional degree of freedom.

The Hamiltonian describing the junction is given by

$$H = \underbrace{H_t + H_b + H_{QSL}}_{H_0} + H_{tb}, \qquad (1)$$

where H_t and H_b are the Hamiltonians of the top and bottom graphene layers, respectively, H_{QSL} characterizes the QSL serving as a tunneling barrier, and H_{tb} is the tunneling Hamiltonian.

The specific form of H_{QSL}, which determines the low-energy excitations responsible for the inelastic electron scattering during tunneling, is not crucial for our derivations and will be discussed in Sec. IV. This flexibility makes our proposal suitable for exploring a wide range of magnetic materials beyond QSLs.

We model each graphene layer as a gas of massless Dirac particles around the valley K_ℓ, where $\ell = \{t, b\}$ labels the layer. This approximation holds for energies up to a few hundred meV and for disorder and interaction strengths that do not induce significant intervalley scattering. We will discuss at the end of this section how to correctly account for electrons

in the vicinity of the K'_ℓ valley. The Hamiltonian of the ℓ layer is

$$H_\ell = \hbar v_F \sum_{k,\alpha,\beta,s} [\tau_{\alpha\beta} \cdot (k + K_\ell) - \mu_\ell] c^\dagger_{k,s,\alpha,\ell} c_{k,s,\beta,\ell}, \quad (2)$$

where $c^\dagger_{k,s,\alpha,\ell}$ creates an electron in sublattice $\alpha = \{A, B\}$ with momentum k and spin $s = \{\uparrow, \downarrow\}$. The Pauli matrices τ act on the sublattice degree of freedom, $v_F \approx 10^6 \text{ ms}^{-1}$ is the Fermi velocity of graphene, and μ_ℓ is the chemical potential of layer ℓ measured from the charge neutrality point of the layer. In Eq. (2), the momentum k in each layer is measured with respect to the Dirac point K_ℓ. Due to the twist angle θ, K_b and K_t do not coincide, i.e., $\Delta K = K_b - K_t = K_b - R(\theta)K_b$, where $R(\theta)$ is the matrix implementing a rotation by an angle θ.

The real-space tunneling Hamiltonian is given by [42]

$$H_{tb} = \frac{1}{\sqrt{N}} \sum_{R_t, R_b} \sum_{\alpha,\beta,s,s'} \Gamma_{ss'}(\Delta r) \quad (3)$$
$$\times c^\dagger_{R_t,\alpha,s,t} c_{R_b,\beta,s',b} e^{ieV_{tb}t/\hbar} + \text{H.c.},$$

where R_t and R_b are the unit-cell position in the top and bottom layer, respectively, and the voltage bias across the junction is incorporated as a time-dependent hopping process. The tunneling matrix $\Gamma_{ss'}(\Delta r)$ is a function of the in-plane distance between the initial and final positions of the electron, denoted as $\Delta r = (R_t + r_{t,\alpha}) - (R_b + r_{b,\beta})$. Here, $r_{\alpha\ell}$ represents the location of the sublattice α within the unit cell of layer ℓ. $\Gamma_{ss'}(\Delta r)$ consists of a bare tunneling term, where the electron does not interact with the QSL, and a term describing tunneling via an exchange-mediated excitation of the QSL:

$$\Gamma_{ss'}(\Delta r) = \Gamma_0(\Delta r) \delta_{s,s'} + \Gamma_1(\Delta r) \sigma_{ss'} \cdot s(r_m). \quad (4)$$

The Pauli matrices σ act on the spin degree of freedom of the electrons in the leads, and $s(r_m)$ represents the local magnetic moment in the insulating barrier at $r_m = (R_t + r_{t,\alpha} + R_b + r_{b,\beta})/2$. This tunneling matrix provides an accurate description when the exchange energy $\approx J_g|s|$ is smaller than the spin-independent barrier height Φ. In this limit, we have $\Gamma_1/\Gamma_0 \approx J_g/\Phi$, with J_g the exchange coupling between the graphene's electrons and the magnetic moments of the QSL [38,39].

In Eq. (4), we assumed that the scattering from the localized spins occurs at the midpoint r_m, neglecting the microscopic details of the barrier. This assumption simultaneously maximizes the transition amplitudes from the top and bottom graphene layers to the magnetic barrier [42]. Additionally, we neglected Kondo interactions between the localized moments and the conducting electrons of each layer. This assumption is justified in the limit of low density in the leads and strong magnetic correlations in the QSL. Lastly, we did not include the effect of Ruderman-Kittel-Kasuya-Yosida (RKKY) interactions, which is a good approximation when the QSL's lattice constant a_{QSL} is larger than that of graphene

$a_g = 2.46 \text{ Å}$. In this case, these interactions are random in sign and weak compared to the magnetic correlations.

We can Fourier transform Eq. (3) and obtain

$$H_{tb} = \frac{1}{\sqrt{N}} \sum_{k,k'} \sum_{g_t, g_b} \sum_{\alpha,\beta,s,s'} e^{i(g_t \cdot r_{\alpha t} - g_b \cdot r_{\beta b})}$$
$$\times [\Gamma_0(q') \delta_{s,s'} \delta_q + \Gamma_1(q') \sigma_{ss'} \cdot s_q] \quad (5)$$
$$\times c^\dagger_{k,\alpha,s,t} c_{k',\beta,s',b} e^{ieV_{tb}t/\hbar} + \text{H.c.},$$

with $q' = (k + k' + K_t + K_b + g_t + g_b)/2$ and $q = k - k' + K_t - K_b + g_t - g_b$. Here, g_t and g_b are the reciprocal lattice vectors of the top and bottom graphene layer, respectively. Note that the momenta q and q' are measured from the center of the Brillouin zone Γ. Instead, k and k' are measured from K_t and K_b, respectively. As in Eq. (2), we consider the tunneling of electrons in the vicinity of the K valleys and hence assume small k and k'. At the end of this section, we will comment on how to correctly account for the tunneling of electrons around the K' valley.

As in the Bistritzer-MacDonald model for twisted bilayer graphene [70], the tunneling functions $\Gamma_0(q')$ and $\Gamma_1(q')$ rapidly decay as a function of $|q'|$ since the vertical separation of the leads exceeds the in-plane lattice constant [42,70]. We thus consider only the components of the tunneling matrix near the Dirac points of the unrotated graphene layers, i.e., $|q'| \approx |K_t + K_b|/2$, and denote the momentum-independent tunneling amplitudes as $\bar{\Gamma}_0$ and $\bar{\Gamma}_1$. This simplification constrains the sum over reciprocal lattice vectors in Eq. (5) and we obtain

$$H_{tb} = \frac{1}{\sqrt{N}} \sum_{k,q} \sum_{\alpha,\beta,s,s'} \sum_{n=0}^{2} [\bar{\Gamma}_0 \delta_{s,s'} \delta_{q,\Delta K_n} + \bar{\Gamma}_1 \sigma_{ss'} \cdot s_{q_n}]$$
$$\times T^{(n)}_{\alpha\beta} (c^\dagger_{k,\alpha,s,t} c_{k-q,\beta,s',b} e^{ieV_{tb}t/\hbar}$$
$$+ c^\dagger_{k-q,\alpha,s,b} c_{k,\beta,s',t} e^{-ieV_{tb}t/\hbar}), \quad (6)$$

with $q_n = q + \Delta K_n$, and ΔK_n denotes the separation of the Dirac cones of the top and bottom layers at the three K valleys in the Brillouin zone. These three vectors are related by a $120°$ rotation, i.e., $\Delta K_n = R(2\pi n/3)\Delta K$. The tunneling matrices are

$$T^{(n)} = \tau^0 + \cos\left(\frac{2\pi n}{3}\right)\tau^x - \sin\left(\frac{2\pi n}{3}\right)\tau^y. \quad (7)$$

For a sufficiently large barrier height, the tunneling Hamiltonian H_{tb} acts as a perturbation and the current flowing through the heterostructure can be computed using linear response theory:

$$I(eV_{tb}) = \frac{i}{\hbar} \int_{-\infty}^{+\infty} dt' \theta(t - t') \langle [H_{tb}(t'), I_{tb}(t)] \rangle. \quad (8)$$

The current operator in Eq. (8) is given by

$$I_{tb} = \frac{ie}{\hbar}[H_{tb}, N_t]$$

$$= -\frac{ie}{\hbar\sqrt{N}} \sum_{k,q} \sum_{\alpha,\beta,s,s'} \sum_{n=0}^{2} [\bar{\Gamma}_0 \delta_{s,s'} \delta_{q,\Delta K_n} + \bar{\Gamma}_1 \sigma_{ss'} \cdot s_{q_n}]$$

$$\times T_{\alpha\beta}^{(n)} (c_{k,\alpha,s,t}^\dagger c_{k-q,\beta,s',b} e^{ieV_{tb}t/\hbar}$$

$$- c_{k-q,\alpha,s,b}^\dagger c_{k,\beta,s',t} e^{-ieV_{tb}t/\hbar}). \quad (9)$$

The current consists of two distinct contributions: direct tunneling, which leaves the magnetic moments of the barrier unperturbed, and a spin-flip process proportional to the spin fluctuations of the QSL. The direct tunneling contribution is given by (see Appendix A)

$$I^{(0)}(eV_{tb}) = \frac{4e\bar{\Gamma}_0^2}{\hbar} \sum_{n=0}^{2} \mathcal{A}^{tb}(\Delta K_n, eV_{tb}, n). \quad (10)$$

The spin-dependent part, instead, is (see Appendix A)

$$I^{(2)}(eV_{tb}) = -\frac{2e\bar{\Gamma}_1^2}{\hbar} \int_{-\infty}^{+\infty} d\omega [n_B(\omega) - n_B(\omega + eV_{tb})]$$

$$\times \sum_n \sum_q \mathcal{S}(q_n, eV_{tb} + \omega) \mathcal{A}^{tb}(q, -\omega, n), \quad (11)$$

where n_B is the Bose-Einstein distribution. The excitations of the QSL are described by the dynamical spin structure factor $\mathcal{S}(q, \omega) = \sum_\gamma \mathcal{S}^\gamma(q, \omega)$ defined as $\mathcal{S}^\gamma(q, \omega) \overset{i\omega \to \omega + i\epsilon^+}{=} -\frac{1}{\pi} \text{Im}\mathcal{G}_s^\gamma(q, i\omega_n)$, with

$$\mathcal{G}_s^\gamma(q, i\omega_n) = -\int_0^\beta d\tau \, e^{i\tau\omega_n} \sum_{ij} e^{iq\cdot(r_i - r_j)} \langle \mathcal{T} s_i^\gamma(\tau) s_j^\gamma \rangle. \quad (12)$$

Here, ω_n are bosonic ($= 2n\pi/\beta$) Matsubara frequencies. We will further characterize the spin structure factor in Sec. IV.

In Eqs. (10) and (11), we introduced the spectral function $\mathcal{A}^{tb}$ which describes the particle-hole excitations in the graphene layers and is defined as

$$\mathcal{A}^{tb}(q, \omega, n) = \frac{\pi}{N} \sum_{k,\lambda,\lambda'} \int_{-\infty}^{+\infty} d\epsilon [n_F(\epsilon) - n_F(\epsilon + \omega)]$$

$$\times \left| T_{k,k-q;\lambda,\lambda'}^{(n)} \right|^2 \mathcal{A}_\lambda^t(k, \epsilon) \mathcal{A}_{\lambda'}^b(k - q, \epsilon + \omega). \quad (13)$$

Here, $\mathcal{A}_\lambda^\ell(k, \omega)$ represents the spectral function of band λ in the graphene layer ℓ, and n_F is the Fermi-Dirac distribution. The tunneling matrix $T_{k,k-q;\lambda,\lambda'}^{(n)}$ is obtained by projecting Eq. (7) onto the eigenbasis of the graphene layers:

$$T_{k,k-q;\lambda,\lambda'}^{(n)} = \langle \psi_\lambda(k)|T^{(n)}|\psi_{\lambda'}(k-q)\rangle$$

$$= \frac{1}{2}[1 + \lambda e^{i(\frac{2\pi n}{3} + \phi_k)}][1 + \lambda' e^{-i(\frac{2\pi n}{3} + \phi_{k-q})}], \quad (14)$$

where $|\psi_\lambda(k)\rangle = (\lambda e^{-i\phi_k}, 1)^T/\sqrt{2}$ represents the eigenvector of Eq. (2) in band λ at momentum $k = |k|e^{i\phi_k}$.

While the graphene layers are C_{6z} symmetric, the candidate QSL material may lack this symmetry. This consideration requires to be careful when computing the additional contribution to the inelastic tunneling stemming from the electrons

in the vicinity of the K' valleys. The shift of the Dirac cones at the K' valley is opposite to that at the K one, i.e., $\Delta K_n' = -\Delta K_n$. Therefore, to account for the contribution from the opposite valley, it is not sufficient to multiply by a valley degeneracy factor $g_v = 2$. Instead, we have to substitute $\mathcal{S}(q + \Delta K_n)$ in Eq. (11) with $\mathcal{S}(q - \Delta K_n)$.

In general, we expect an additional contribution to the total current that is linear in the magnetic moment of the barrier $\langle s_{q_n} \rangle$. However, this term vanishes when the leads are not spin polarized (see Appendix A) [39]. Our primary objective is to investigate the properties of QSLs, with a particular emphasis on measuring the spin structure factor $\mathcal{S}(q, \omega)$ rather than $\langle s_{q_n} \rangle$. The absence of an additional current term linear in $\bar{\Gamma}_1$ is advantageous for our purposes. Nevertheless, the use of spin-polarized leads would offer the opportunity to probe individual components of $\mathcal{S}(q, \omega)$ [71].

III. INELASTIC ELECTRON TUNNELING SPECTROSCOPY AND THE SPIN STRUCTURE FACTOR

Equations (10) and (11) provide a general description of the current flowing through the heterostructures, accounting for finite temperature, disorder, and interactions in the leads. Our objective is to establish a simple analytical relation that directly connects the dynamical spin structure factor $\mathcal{S}(q, \omega)$ with a measurable quantity in the tunneling heterostructure. To achieve this, we make a series of simplifying approximations.

To distinguish the features of fractionalized excitations from the thermal broadening of magnons in magnetically ordered materials [71], one has to consider a regime where the thermal energy $k_B T$ is much smaller than the characteristic magnetic correlations J within the tunneling barrier, i.e., $k_B T \ll J$. Therefore, we consider the limit of zero temperature in the subsequent analysis. The expression for the spin-dependent current simplifies as follows:

$$I_{T=0}^{(2)}(eV_{tb}) = \frac{2e\bar{\Gamma}_1^2}{\hbar} \int_0^{eV_{tb}} d\omega \sum_n \sum_q \mathcal{S}(q_n, \omega)$$

$$\times \mathcal{A}^{tb}(q, eV_{tb} - \omega, n), \quad (15)$$

with

$$\mathcal{A}_{T=0}^{tb}(q, \omega, n) = \frac{\pi}{N} \sum_{k,\lambda,\lambda'} \int_0^\omega d\epsilon \left| T_{k,k-q;\lambda,\lambda'}^{(n)} \right|^2$$

$$\times \mathcal{A}_\lambda^t(k, \epsilon - \omega) \mathcal{A}_{\lambda'}^b(k - q, \epsilon). \quad (16)$$

The current is a convolution of the spin structure factor $\mathcal{S}(q_n, \omega)$ and the particle-hole spectral function $\mathcal{A}_{T=0}^{tb}(q, \omega, n)$ which is a property of the graphene layers. This convolution acts as a frequency-dependent smearing of the momentum at which we probe $\mathcal{S}$.

Let us consider electron-doped graphene layers and further assume $\mu_t = \mu_b \gg eV_{tb}$. This situation can be achieved by independently controlling the bottom and top gates of the tunneling junction. The largest momentum transfer $|q|$ is then $|q_{max}| \approx 2\mu/\hbar v_F$. If we focus on sufficiently large twist angles, i.e., $2\mu/\hbar v_F|\Delta K| \ll 1$, we can disregard the smearing in Eq. (15). Namely, we ignore the momentum transfer q

between the graphene layers and the QSL, and carry the sum over q past $\mathcal{S}(q_n, \omega)$.

The scattering matrix $T_{k,k-q}^{(n)}$ depends exclusively on the angles ϕ_k and ϕ_{k-q} [cf. Eq. (14)], and is unity once averaged over the angular variables. We can then use $1/N \sum_k \mathcal{A}(k, \epsilon) = \mathcal{N}(\epsilon)$, where $\mathcal{N}(\epsilon) = \sqrt{3} a_g^2 |\mu + \epsilon|/(4\pi \hbar^2 v_F^2)$ is the particle density of the graphene layer. In the limit $\mu \gg eV_{tb}$, we neglect the energy dependence of the graphene's density of state and reach a simple expression for the spin-dependent tunneling current:

$$I_{T=0}^{(2)}(eV_{tb}) = -\frac{3ea_g^2 L^2 \bar{\Gamma}_1^2 \mu^2}{8\pi \hbar^5 v_F^4} \sum_n$$
$$\times \int_0^{eV_{tb}} d\omega\, \mathcal{S}(\Delta K_n, \omega)(eV_{tb} - \omega), \quad (17)$$

where L is the in-plane linear size of the graphene layers.

The scattering from the excitations of the QSL opens new inelastic channels for the electrons tunneling between the graphene layers. This should result in a clear signature in the inelastic electron tunneling spectroscopy. Taking the second derivative of Eq. (17), we obtain the spin-dependent contribution to the IETS signal:

$$\frac{d^2 I_{T=0}^{(2)}(eV_{tb})}{dV_{tb}^2} = -\frac{3e^3 a_g^2 L^2 \bar{\Gamma}_1^2 \mu^2}{8\pi \hbar^5 v_F^4} \sum_n \mathcal{S}(\Delta K_n, eV_{tb}). \quad (18)$$

By measuring the IETS signal in a quantum twisting microscope with a magnetic insulator acting as the tunneling barrier, it becomes possible to directly probe the spectrum of magnetic excitations. The control of the voltage bias between the graphene layers and the relative twist angle between them gives access to the energy and momentum dependence of the spin structure factor, respectively.

While Eq. (11) is a generic result that relies on few physically motivated assumptions and constitutes a rigorous starting point for a comparison with future experimental data, Eq. (18) is a simple analytical relation resting on a series of additional assumptions. Specifically, it holds at zero temperature, for large twist angles, and for voltage biases much smaller than the graphene's chemical potential. These limits capture the regime where the IETS signal can be directly linked to the spin structure factor of the barrier, as described by Eq. (18).

In Appendix B, we compute the current stemming from direct tunneling and show that direct tunneling also contributes to the IETS signal [37]. The spin-independent contribution, however, is only present for voltages simultaneously satisfying $eV_{tb} < \hbar v_F |\Delta K| < eV_{tb} + 2\mu$. Considering that the relevant energy scale of the QSL is expected to be on the order of tens of meV, the large Fermi velocity of graphene ensures that a significant region of the $eV_{tb} - \theta$ diagram exclusively contains the IETS signal originating from the QSL contribution. This is clearly depicted in Fig. 2, where the gray region shades the area where the direct tunneling contributes. Note that it is also the region where the simplifying assumptions made to reach Eq. (18) break down.

The energy resolution of the quantum twisting microscope is set by the measurement temperature. Preliminary results have been obtained with a quantum twisting microscope
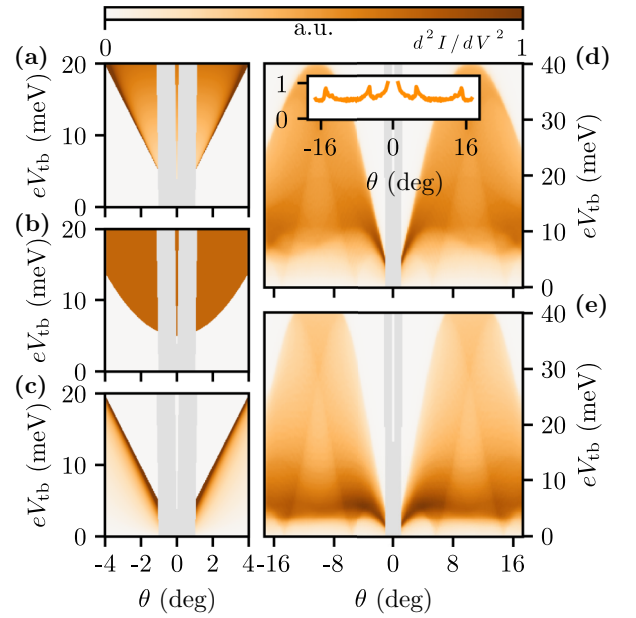

FIG. 2. Inelastic electron tunneling spectroscopy signal for various QSLs in a quantum twisting microscope: (a) a Dirac QSL, (b) a gapped QSL, and (c) a QSL with a spinon Fermi surface with a parabolic spinon band. For the evaluation of the IETS signal, we assumed $v_s = 2.5 \times 10^4 \, \text{ms}^{-1}$, $\Delta_s = 30 \, \text{meV}$, $m_s \approx 3m_e$, and $\mu = 100 \, \text{meV}$. (d), (e) Present the IETS signal of a QSL with a spinon Fermi surface obtained by a spinon tight-binding model on a triangular lattice with and without next-to-nearest-neighbor hoppings, respectively. The inset in (d) shows the IETS signal at zero-bias voltage. Here, we assumed $t_s = 5 \, \text{meV}$ and $\chi_s = 1 \, \text{meV}$ for the spinon hopping. The gray region shades the area where elastic tunneling contributes to the IETS signal.

operating at 4 K [72,73]. While this temperature is already significantly lower than the magnetic interactions in many candidate QSL materials, reaching even lower temperatures will be crucial to conclusively probe the excitations of these materials. The momentum resolution on ΔK depends on the ability to control the twist angle of the leads. Previous studies [37] achieved a resolution of $\delta\theta \approx 0.001°$, which corresponds to $\delta|\Delta K| \approx 3 \times 10^{-5} \, \text{Å}^{-1}$. The main uncertainty in probing the spin-structure factor at a definite momentum, however, stems from precisely accounting for the convolution with the graphene's particle-hole spectral function in Eq. (15). There are two main factors that limit the momentum resolution. First, the in-plane linear size L of the graphene layers sets a limit of $\delta|q| \approx 1/L$. Second, via the convolution in Eq. (15), the signal is smeared over the Fermi surface of the graphene layers with a resolution $\delta|q| \approx 2\mu/\hbar v_F$. It would appear that the best resolution is achieved when both graphene layers are maintained at charge neutrality. Nonetheless, in this configuration, one cannot neglect the linear dependence in energy of the graphene's density of state. The energy convolution in Eq. (17) would then be with the cubic rather than linear power of $(eV_{tb} - \omega)$, and only the fourth derivative of the current with respect to the voltage bias would be directly proportional to the spin structure factor. Instead, one could use a two-dimensional metal with a small Fermi pocket at valley K and achieve similar results to those discussed here for doped

graphene. Lastly, we neglected any spatial inhomogeneity in the graphene layers, that can in principle modulate the tunneling amplitude on a length scale ℓ. If present, they would further reduce the momentum resolution by roughly $1/\ell$.

The maximum momentum that can be probed is approximately $|\Delta \boldsymbol{K}|_{\max} = 2|\boldsymbol{K}| \sin \theta_{\max}/2$, with previous studies reaching up to $\theta_{\max} = 30°$ [72,73]. Given that the unit cell of graphene is often smaller than that of candidate QSL materials, even small twist angles should be able to explore a significant portion of the QSL Brillouin zone (BZ). For example, for 1T-TaS$_2$ we have $a_{\mathrm{QSL}} \approx 12.11$ Å and an angle $\theta \approx 11.7°$ suffices to probe the corners of the BZ. By tuning the twist angle between the graphene layers, it is possible to probe line cuts in the Brillouin zone of the candidate QSL material. To fully map the angular dependence of the spin structure factor, however, it would be desirable to also control the angle between graphene and the QSL barrier.

IV. DISTINGUISHING VARIOUS QUANTUM SPIN LIQUIDS

To analyze different types of QSLs, we adopt a phenomenological approach by using a slave-particle mean-field Hamiltonian [1,74–78]. While this approach may not capture the precise details of specific materials, its main purpose is to demonstrate the efficacy of a quantum twisting microscope in distinguishing between various QSLs. Importantly, the key result represented by Eq. (18) remains valid regardless of the specific details of the QSL Hamiltonian or the methods employed to compute the spin structure factor $\mathcal{S}(\boldsymbol{q}, \omega)$.

We consider a tunneling barrier described by a Hamiltonian quadratic in the spin degree of freedom, such as a Heisenberg Hamiltonian. To describe the physical spins, we utilize a fermionic representation in terms of Abrikosov fermions and decouple the quartic term in the spinon operators via a mean-field approximation. The dynamical spin structure factor can be directly computed using the definition of Eq. (12) (see Appendix C). For instance, in the case of a U(1) QSL, it is given by

$$\mathcal{S}(\boldsymbol{q}, \omega) = \frac{1}{4N} \sum_{ss'} \sum_{\boldsymbol{k}} \sum_{nl} g_{ss'}(\boldsymbol{k}, \boldsymbol{q}, n, l)(2 - \delta_{ss'})$$
$$\times \left[n_{\mathrm{F}}(\xi_{n\boldsymbol{k}}^s) - n_{\mathrm{F}}(\xi_{l\boldsymbol{k}+\boldsymbol{q}}^{s'}) \right] \delta(\omega - \xi_{n\boldsymbol{k}}^s + \xi_{l\boldsymbol{k}+\boldsymbol{q}}^{s'}), \quad (19)$$

where $\xi_{n\boldsymbol{k}}^s$ is the energy at momentum $\boldsymbol{k}$ of the band n with spin s of the spinon mean-field Hamiltonian. The associated eigenvector at sublattice α is $U_{\alpha ns}(\boldsymbol{k})$. The form factor $g_{ss'}(\boldsymbol{k}, \boldsymbol{q}, n, l)$ accounts for the overlap of the eigenstates' wave functions:

$$g_{ss'}(\boldsymbol{k}, \boldsymbol{q}, n, l) = \left| \sum_{\alpha} e^{i\boldsymbol{q}\cdot\boldsymbol{\delta}_{\alpha}} U_{\alpha ns}^*(\boldsymbol{k}) U_{\alpha ls'}(\boldsymbol{k}+\boldsymbol{q}) \right|^2, \quad (20)$$

where $\boldsymbol{\delta}_{\alpha}$ is the position of sublattice α within the unit cell. The form factor plays an important role in multiband spinon models, whereas we will neglect it in the low-energy and single-band models analyzed below.

The dynamical spin structure factor describes spinon particle-hole excitations rather than a single quasiparticle with a well-defined dispersion, as it would be for magnons in magnetically ordered materials. In fact, spin-flip excitations must have integer spin while spinons have fractional spin.

Consequently, the energy and momentum of the excitation are shared between two quasiparticles, leading to a broad continuum of excitations rather than a sharp dispersion. This broad continuum in the excitation spectrum is characteristic of QSL behavior.

Now, let us consider three qualitatively distinct quantum spin liquids: a Dirac spin liquid, a gapped chiral QSL, and a gapless QSL with a spinon Fermi surface. For each case, we derive the dynamical spin structure factor $\mathcal{S}(\boldsymbol{q}, \omega)$ in the long-wavelength and low-energy limit at zero temperature [19].

Let us start with the Dirac spin liquid. Its low-energy dispersion is given by $\xi_{n\boldsymbol{k}} = n\hbar v_{\mathrm{s}}|\boldsymbol{k}|$, with $n = \pm$ and v_{s} the spinon Fermi velocity. The dynamical spin structure factor for this case is obtained as

$$\mathcal{S}(\boldsymbol{q}, \omega) = \frac{3\Omega}{2} \int \frac{\mathrm{d}^2\boldsymbol{k}}{(2\pi)^2} \delta(\omega - \hbar v_{\mathrm{s}}|\boldsymbol{k}| - \hbar v_{\mathrm{s}}|\boldsymbol{k}+\boldsymbol{q}|)$$
$$= \frac{3\Omega}{16\pi \hbar^2 v_{\mathrm{s}}^2} \frac{\omega^2 - \hbar^2 v_{\mathrm{s}}^2 q^2/2}{\sqrt{\omega^2 - \hbar^2 v_{\mathrm{s}}^2 q^2}} \Theta(\omega - \hbar v_{\mathrm{s}} q), \quad (21)$$

where Ω is the unit-cell area of the QSL. Note that this expression equally applies to the case of $\mathbb{Z}_2$ Dirac spin liquids. The spin structure factor given by Eq. (21) exhibits a square-root singularity as ω approaches $\hbar v_{\mathrm{s}} q^+$ and a threshold at $\omega > \hbar v_{\mathrm{s}} q$, which is determined by the spinon Fermi velocity [cf. Fig. 2(a)].

In the case of gapped chiral QSLs, we assume that the spinon dispersion has a minimum at $\boldsymbol{k} = 0$ for the conduction band and a maximum for the valence band at the same location. The low-energy dispersion is given by $\xi_{n\boldsymbol{k}} = n(\hbar^2\boldsymbol{k}^2/2m_{\mathrm{s}} + \Delta_{\mathrm{s}}/2)$, where $n = \pm$. Δ_{s} is the gap in the spinon spectrum and m_{s} is the spinon mass. The dynamical spin structure factor is obtained as

$$\mathcal{S}(\boldsymbol{q}, \omega) = \frac{3\Omega}{2} \int \frac{\mathrm{d}^2\boldsymbol{k}}{(2\pi)^2} \delta\left(\omega - \Delta_{\mathrm{s}} - \frac{\hbar^2 k^2}{2m_{\mathrm{s}}} - \frac{\hbar^2(\boldsymbol{k}+\boldsymbol{q})^2}{2m_{\mathrm{s}}}\right)$$
$$= \frac{3m_{\mathrm{s}}\Omega}{8\pi\hbar^2} \Theta\left(\omega - \Delta_{\mathrm{s}} - \frac{\hbar^2 q^2}{4m_{\mathrm{s}}}\right). \quad (22)$$

The result holds for gapped $\mathbb{Z}_2$ QSLs as well. The spin structure factor described by Eq. (22) exhibits a steplike behavior with a threshold at $\omega > \Delta_{\mathrm{s}} + \hbar^2 q^2/4m_{\mathrm{s}}$, as depicted in Fig. 2(b).

Finally, let us consider a gapless QSL with a spinon Fermi surface. We approximate the spinon dispersion with a parabola and consider the limit $|\boldsymbol{q}| \ll k_{\mathrm{s,F}}$, where $k_{\mathrm{s,F}}$ is the spinon Fermi momentum. The spin structure factor is given by [79]

$$\mathcal{S}(\boldsymbol{q}, \omega) = \frac{3}{2} \frac{1}{2k_{\mathrm{s,F}} q_n} \int_{\substack{k < k_{\mathrm{s,F}} \\ |\boldsymbol{k}+\boldsymbol{q}| > k_{\mathrm{s,F}}}} \frac{\mathrm{d}^2\boldsymbol{k}}{(2\pi)^2}$$
$$\times \delta\left(\omega + \frac{\hbar^2 k^2}{2m_{\mathrm{s}}} - \frac{\hbar^2(\boldsymbol{k}+\boldsymbol{q})^2}{2m_{\mathrm{s}}}\right)$$
$$= \frac{3}{8\pi^2\hbar q v_{\mathrm{s}}} \frac{\omega}{\sqrt{\hbar^2 v_{\mathrm{s}}^2 q^2 - \omega^2}} \Theta(\hbar v_{\mathrm{s}} q - \omega), \quad (23)$$

where $v_s = \hbar k_{s,F}/m_s$ and m_s is the effective mass of the spinons. The spin structure factor, shown in Fig. 2(c), decreases linearly at small frequencies and has a finite signal only for $\omega < \hbar v_s q$.

By analyzing the IETS signal in the quantum twisting microscope, we can qualitatively distinguish between various QSLs. Since the direct tunneling dominates at small twist angle and large voltage bias, it is beneficial to control the twist angle to access the large-angle regime where the inelastic contribution prevails at low voltage biases, as shown in Fig. 2. Examining how the IETS signal evolves at low applied bias voltage allows to differentiate among different quantum spin liquids, as discussed in the previous paragraphs [19,42]. While Ref. [43] first showed the possibility to single out the IETS signal of a gapped QSL in a planar tunneling junction lacking the twist angle tuning knob, at odds with previous proposals [42,43,43], the additional momentum resolution provided by the twist angle allows to also extract low-energy parameters of the spinon Hamiltonian, such as the effective mass and the Fermi velocity of the spinons.

To further prove how the momentum resolution offers insights into the underlying Hamiltonian of the QSL, let us consider a QSL with a spinon Fermi surface on a triangular lattice. This state has been suggested to be a good description for the putative QSL in 1T-TaS$_2$ [61]. At the mean-field level, this state can be described by a nearest-neighbor tight-binding model for spinons on the triangular lattice [80]. The spinon energy is spin independent and given by $\xi_{\boldsymbol{k}} = -2t_s[\cos{(k_x)} + 2\cos{(\frac{k_x}{2})}\cos{(\frac{\sqrt{3}k_y}{2})}] - \mu_s$, where t_s is the spinon hopping parameter, and the chemical potential $\mu_s = 0.8346\,t_s$ ensures half-filling of the spinon bands. We consider a spinon hopping $t_s = 5\,\text{meV}$. Note that the actual value for 1T-TaS$_2$ is currently unknown. Attempts to fit the residual temperature-independent static spin susceptibility and specific heat measured in 1T-TaS$_2$ [62,81] to a simple mean-field spinon model [61] result in an order of magnitude larger spinon hopping parameter. These measurements, however, were carried out in bulk samples and it is unclear whether they should be linked to a QSL model [65–68]. STM studies reporting evidence of QSL behavior in the closely related 1T-TaSe$_2$ monolayer, instead, put an upper bound of 5 meV on the in-plane exchange coupling [45,46]. While at the present time we cannot reliably estimate the physical value of t_s, we stress that our proposal works best for QSLs with a small exchange coupling. Namely, a larger separation in the QSL's and graphene's energy scales improves the validity of the approximations that led to Eq. (18) and increases the area in the $eV_{tb} - \theta$ diagram where the IETS signal is dominated by the QSL contribution. Note also that the spinon spectral signatures takes place at voltage biases smaller than the charge gap, e.g., 400 meV for 1T-TaS$_2$. Therefore, spinon excitations can be easily separated from charge excitations. The IETS signal arising from this state, as obtained from Eqs. (19) and (18), is shown in Fig. 2(d). The inset shows the IETS signal at zero voltage bias. It proves how the IETS signal as a function of the twist angle can determine the spinon Fermi momentum. In fact, the peaks of the IETS signal at zero voltage bias and nonzero twist angle correspond to $2|\boldsymbol{K}|\sin(\theta/2) = |2\boldsymbol{k}_{F,s} + \boldsymbol{b}_i|$, where $\boldsymbol{b}_i$ is a QSL reciprocal lattice vector.

An additional next-nearest-neighbor hopping term for the spinons represents a minimal modification to the previous model [80]. The new energy dispersion is given by $\xi'_{\boldsymbol{k}} = \xi_{\boldsymbol{k}} - 2\chi_s[\cos{(\sqrt{3}k_y)} + 2\cos{(\frac{3k_x}{2})}\cos{(\frac{\sqrt{3}k_y}{2})}]$, and the chemical potential is adjusted to maintain half-filling. The resulting IETS signal is shown in Fig. 2(e). We observe a significant shift of weight towards lower voltage biases. While this example is particularly simple, it illustrates how the experimentally measurable IETS signal, when compared to different microscopic theories, contains sufficient information to better constrain the Hamiltonian of the underlying QSL material. Ultimately, the finite resolution may limit the ability to precisely determine the microscopic parameters, but the possibility to map the spin structure factor in both momentum and energy space presents a substantial advantage over existing probes for QSL materials in monolayer and few-layer materials.

In Fig. 2, we presented the IETS signal expected in a quantum twisting microscope according to Eq. (18). These results have been obtained fixing the chemical potential of the graphene layers to $\mu = 100\,\text{meV}$, which meets the condition $\mu \gg eV_{tb}$ for the voltage biases considered. Nonetheless, such a large value of the chemical potential carries unwanted consequences. To reach Eq. (18) from Eq. (15), we neglected the momentum transfer to the QSL $\boldsymbol{q}$, whose maximum value is $\delta q = 2\mu/\hbar v_F \approx 3 \times 10^{-2}\,\text{Å}^{-1}$, or alternatively $\delta\theta \approx 0.7°$. Here, we show how relaxing the condition $\mu \gg eV_{tb}$ to $\mu \geqslant eV_{tb}$ allows to reduce the uncertainty on momentum and still distinguish among various QSLs.

By requiring $\mu \geqslant eV_{tb}$, we can still restrict our attention to scattering involving only electrons in the upper band, but we cannot ignore the linear-in-energy density of state of graphene. In this case, we obtain

$$\frac{d^2 I_{T=0}^{(2)}(eV_{tb})}{dV_{tb}^2} = -\frac{3e^3 a_g^2 L^2 \bar{\Gamma}_1^2}{8\pi \hbar^5 v_F^4} \sum_n \left[\mu^2 \mathcal{S}(\Delta\boldsymbol{K}_n, eV_{tb}) - \int_0^{eV_{tb}} d\omega\, \mathcal{S}(\Delta\boldsymbol{K}_n, \omega)(eV_{tb} - \omega) \right]. \quad (24)$$

In Fig. 3, we compare the IETS signal at a fixed angle $\theta = 2°$ obtained by Eq. (18) and by Eq. (24) with $\mu = 20\,\text{eV}$. The chemical potential $\mu = 20\,\text{meV}$ corresponds to an error $\delta\boldsymbol{q} \approx 6 \times 10^{-3}\,\text{Å}^{-1}$. In Fig. 3(a), we present the result for Dirac QSL, where we can see that while at large voltages the signal differs, we still detect an onset at $eV_{tb} = \hbar v_s|\Delta\boldsymbol{K}|$ with a square-root singularity above it [cf. Eq. (21)]. A similar analysis is displayed in Fig. 3(b) for a gapped chiral QSL. We again observe an onset at $eV_{tb} = \Delta_s + \hbar^2|\Delta\boldsymbol{K}|^2/2m_s$, as expected from Eq. (22), but the signal is no longer constant above it. The absence of a singularity at the onset allows to distinguish this case from that of a Dirac QSL. Lastly, in Fig. 3(c), we present the IETS signal of a QSL with a spinon Fermi surface. Here, the signal ceases to be zero above the threshold $eV_{tb} = \hbar v_s|\Delta\boldsymbol{K}|$. The presence of a finite signal below the threshold with a linear dependence on eV_{tb} at small voltage biases and a square-root singularity when the threshold is approached from below clearly distinguishes this case from the previous ones. In Figs. 3(d) and 3(e), we show that even with Eq. (24) and a smaller chemical potential, it is possible to identify the spinon Fermi wave vector and the
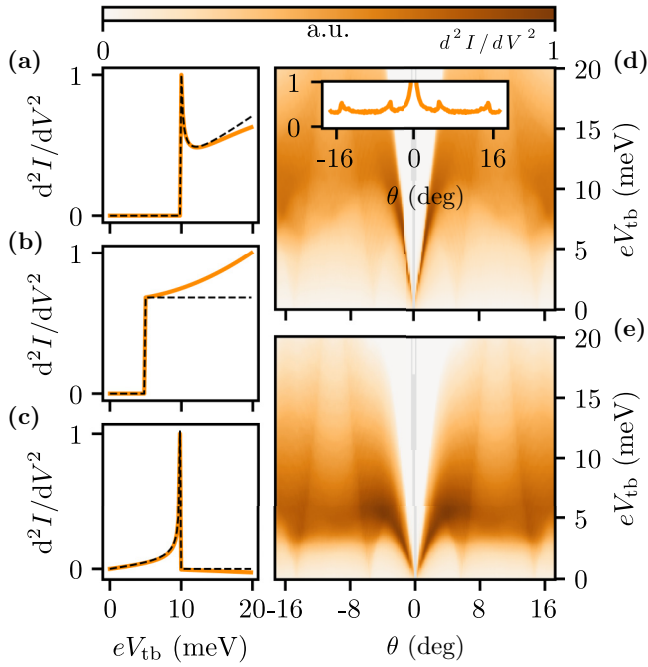
FIG. 3. Inelastic electron tunneling spectroscopy signal with smaller chemical potential: (a) a Dirac QSL, (b) a gapped QSL, and (c) a QSL with a spinon Fermi surface with a parabolic spinon band. For the evaluation of the IETS signal, we assumed the same parameters as in Fig. 2 but $\mu = 20$ meV and fixed the angle at $\theta = 3°$. The black dashed line indicates the IETS signal obtained via Eq. (18), while the orange line the one obtained by Eq. (24). (d), (e) Are analogous to the same panels in Fig. 2 but with IETS signal computed according to Eq. (24) and $\mu = 20$ meV.

shift of the IETS signal at lower voltage biases upon the introduction of next-to-nearest-neighbor hopping in toy model of spinon hopping on a triangular lattice.

Lastly, we note that for QSL with large energy scales, even the condition $\mu \geqslant V_{tb}$ might result in too large δq. In this case, we foresee two possible strategies. On one hand, we could change the chemical potential as a function of the voltage bias such that at low energies, the IETS signal is still well described by Eq. (18) with a small momentum uncertainty. On the other hand, one could numerically solve Eq. (11) in its full generality to compare various theoretical models to the experimental results.

V. DISCUSSIONS AND CONCLUSIONS

In this paper, we introduced the quantum twisting microscope as a promising tool for imaging the excitations of QSLs in two-dimensional materials. One significant advantage of this technique, distinguishing it from previous proposals, is its ability to provide resolution in both momentum and energy. By focusing on simplified limits, we demonstrated that the IETS signal of the tunneling junction has a contribution directly proportional to the dynamical spin structure factor of the tunneling barrier, as shown in Eq. (18).

References [42,43] first proposed to use a planar tunneling junction to probe quantum spin liquids. Reference [43]

showed how to effectively separate between the elastic and inelastic contributions to the tunneling current in this configuration. In their proposal, however, only the zero-momentum spin structure factor of quantum spin liquids with short-range spinon correlations could be probed. Using graphene as metallic leads and introducing a fixed finite twist angle, Ref. [42] showed how to probe the spin structure factor of a Kitaev QSL at finite momentum. Nonetheless, it did not investigate the possibility to continuously vary the twist angle or the signal stemming from different QSLs. Here, motivated by these previous works and the quantum twisting microscope of Ref. [37], we showed how the *in situ* control over the twist angle is an important tuning knob that allows to probe the spin structure factor with energy and momentum resolution. Conceptually, our proposal provides a tool to study candidate QSL materials in the monolayer and few-layer limit in ways that were previously achievable only for bulk materials via inelastic neutron scattering. The additional momentum resolution will allow to extract precious information on the effective parameters of the microscopic Hamiltonian describing the QSL, e.g., the spinon velocity, the Fermi wave vectors, and the spinon mass.

In the following, we briefly discuss the implications of departing from the limits considered in our study and the experimental feasibility of our proposal. Equation (11) is valid at finite temperatures, and in the presence of disorder and interaction in the leads. Moreover, it holds regardless of the approximation used to compute the spin structure factor. While not as simple as Eq. (18), it establishes a starting point for comparing experimental results to theoretical predictions. Additionally, a faithful representation of the experimental conditions requires a careful description of the electrostatics of the junction. In this study, we assumed that the voltage bias through the junction results in a simple electrostatic potential shift. However, in reality, a voltage bias will induce both a shift of the chemical potential and an electrostatic potential between the layers. This more realistic situation can be easily accounted for [37,56,57]. A dual-gated device, with independent control of the gates of the bottom and top graphene layers [37], offers a more direct realization of the present proposal as it allows to maintain fixed chemical potentials and change the relative electrostatic potential shift.

From a fabrication standpoint, substantial progress has been made in the mechanical exfoliation of monolayer and few-layer samples of candidate quantum spin liquids such as α-RuCl$_3$ and 1T-TaS$_2$ [82–87]. Moreover, successful deposition of monolayer graphene onto the surface of these materials has been achieved [7,88–96]. These advancements give us hope that our proposed tunneling junction could be realized in the near future. However, it is worth noting that these interfaces often exhibit significant charge transfer between graphene and the candidate quantum spin liquid due to the difference in the work functions of the materials, i.e., 0.5 eV [95] and 1.5 eV [83] for graphene on 1T-TaS$_2$ and α-RuCl$_3$, respectively. In a dual-gated device, with independent control of the gates of the bottom and top graphene layers, we might hope to mitigate this charge transfer. This strategy seems particularly suitable for 1T-TaS$_2$, where graphene deposited on top of the bulk material gets hole doped by 0.1 eV [95]. Alternatively,

an additional hBN or TMD spacer layer between graphene and the QSL material, e.g., a monolayer on each side of the junction, could further reduce the doping to an acceptable level. The additional layer between the graphene and the candidate QSL material further allows to cap air-sensitive materials like 1T-TaS$_2$ in the glove box and more easily transfer them in the quantum twisting microscope [37].

In conclusion, we presented a proposal to detect the signatures of fractionalized excitations in two-dimensional materials via tunneling spectroscopy in a quantum twisting microscope. Importantly, this technique extends to the monolayer limit and offers both momentum and energy resolution, going beyond the capabilities of current experimental methods to probe magnetic materials.

APPENDIX A: DERIVATION OF THE TUNNELING CURRENT

We here present the derivation of the tunneling current flowing through the junction. Our derivation parallels the one performed in Ref. [42]. Our starting point is the tunneling Hamiltonian

$$H_{\mathrm{tb}} = \frac{1}{\sqrt{N}} \sum_{\mathbf{k},\mathbf{q}} \sum_{\alpha,\beta,s,s'} \sum_{n=0}^{2} T_{\alpha\beta}^{(n)} [\bar{\Gamma}_0 \delta_{s,s'} \delta_{\mathbf{q},\Delta\mathbf{K}_n} + \bar{\Gamma}_1 \boldsymbol{\sigma}_{ss'} \cdot \mathbf{s}_{\mathbf{q}_n}]$$
$$\times (c_{\mathbf{k},\alpha,s,\mathrm{t}}^{\dagger} c_{\mathbf{k}-\mathbf{q},\beta,s',\mathrm{b}} e^{ieV_{\mathrm{tb}}t} + c_{\mathbf{k}-\mathbf{q},\alpha,s,\mathrm{b}}^{\dagger} c_{\mathbf{k},\beta,s',\mathrm{t}} e^{-ieV_{\mathrm{tb}}t}), \tag{A1}$$

where the voltage bias across the tunneling junction is captured by a time-dependent tunneling process. This approach allows us to use equilibrium techniques to compute the tunneling current in linear response theory. The current operator is

$$I_{\mathrm{tb}} = \frac{ie}{\hbar} [H_{\mathrm{tb}}, N_{\mathrm{t}}]$$
$$= -\frac{ie}{\hbar\sqrt{N}} \sum_{\mathbf{k},\mathbf{q}} \sum_{\alpha,\beta,s,s'} \sum_{n=0}^{2} T_{\alpha\beta}^{(n)} [\bar{\Gamma}_0 \delta_{s,s'} \delta_{\mathbf{q},\Delta\mathbf{K}_n} + \bar{\Gamma}_1 \boldsymbol{\sigma}_{ss'} \cdot \mathbf{s}_{\mathbf{q}_n}]$$
$$\times (c_{\mathbf{k},\alpha,s,\mathrm{t}}^{\dagger} c_{\mathbf{k}-\mathbf{q},\beta,s',\mathrm{b}} e^{ieV_{\mathrm{tb}}t} - c_{\mathbf{k}-\mathbf{q},\alpha,s,\mathrm{b}}^{\dagger} c_{\mathbf{k},\beta,s',\mathrm{t}} e^{-ieV_{\mathrm{tb}}t}). \tag{A2}$$

The current through the junction is then given by

$$I = \frac{i}{\hbar} \int_{-\infty}^{+\infty} dt' \theta(t - t') \langle [H_{\mathrm{tb}}(t'), I_{\mathrm{tb}}(t)] \rangle = \frac{2e}{\hbar} \mathrm{Im} \chi_{AA}(eV_{\mathrm{tb}}), \tag{A3}$$

with the time evolution generated by H_0. The operator A is defined as

$$A(t) = \frac{1}{\sqrt{N}} \sum_{\mathbf{k},\mathbf{q}} \sum_{\alpha,\beta,s,s'} \sum_{n=0}^{2} T_{\alpha\beta}^{(n)} [\bar{\Gamma}_0 \delta_{s,s'} \delta_{\mathbf{q},\Delta\mathbf{K}_n} + \bar{\Gamma}_1 \boldsymbol{\sigma}_{ss'} \cdot \mathbf{s}_{\mathbf{q}_n}(t)]$$
$$\times c_{\mathbf{k},\alpha,s,\mathrm{t}}^{\dagger}(t) c_{\mathbf{k}-\mathbf{q},\beta,s',\mathrm{b}}(t), \tag{A4}$$

and the response function χ_{AA} is

$$\chi_{AA}(\omega) = -\frac{i}{\hbar} \lim_{\eta\to 0^+} \int_0^\infty dt \, e^{i(\omega+i\eta)t/\hbar} \langle [A(t), A^{\dagger}(0)] \rangle. \tag{A5}$$

The current can be easily evaluated via the Matsubara formalism. We separately compute the contribution stemming from elastic tunneling $\chi^{(0)}$ and the one from the spin-dependent scattering from the quantum spin liquid $\chi^{(2)}$. To this end, we define as A_0 the spin-independent part of the operator in Eq. (A4) and as A_2 the spin-dependent one.

First, let us consider the elastic tunneling contribution:

$$\chi^{(0)}(i\omega_n) = -\int_0^\beta d\tau \, e^{i\omega_n\tau} \langle \mathcal{T} A_0(\tau) A_0^{\dagger}(0) \rangle$$
$$= -\frac{2\bar{\Gamma}_0^2}{N} \sum_{\mathbf{k}} \sum_{n=0}^{2} \int_0^\beta d\tau \, e^{i\omega_n\tau} \mathrm{Tr}$$
$$\times [\mathcal{G}^{\mathrm{b}}(\mathbf{k} - \Delta\mathbf{K}_n, \tau) T^{(n)} \mathcal{G}^{\mathrm{t}}(\mathbf{k}, -\tau) T^{(n)}], \tag{A6}$$

where we assumed that the two graphene layers are uncorrelated in the absence of the tunneling Hamiltonian. The factor 2 comes from the spin multiplicity, and Tr acts on the orbital space. In Eq. (A6), we introduced the electron Green's functions

$$\mathcal{G}_{\alpha,\alpha'}^{\ell}(\mathbf{k}, -\tau) = -\langle \mathcal{T} c_{\mathbf{k},\alpha',s,\ell}^{\dagger}(\tau) c_{\mathbf{k},\alpha,s,\ell} \rangle, \tag{A7}$$

$$\mathcal{G}_{\alpha,\alpha'}^{\ell}(\mathbf{k}, \tau) = -\langle \mathcal{T} c_{\mathbf{k},\alpha,s,\ell}(\tau) c_{\mathbf{k},\alpha',s,\ell}^{\dagger} \rangle. \tag{A8}$$

We conveniently parametrize the matrices $T^{(n)}$ as

$$T^{(n)} = \tau^0 + \cos\left(\frac{2\pi n}{3}\right)\tau^x - \sin\left(\frac{2\pi n}{3}\right)\tau^y, \tag{A9}$$

and move from orbital to band space. Via a Fourier transform of the electronic Green's functions, we then obtain

$$\chi^{(0)}(i\omega_n) = -\frac{2\bar{\Gamma}_0^2}{N} \sum_{\mathbf{k},\lambda,\lambda'} \sum_{n=0}^{2} |\langle \lambda, \mathbf{k}|T^{(n)}|\lambda', \mathbf{k} - \Delta\mathbf{K}_n\rangle|^2 \frac{1}{\beta}$$
$$\times \sum_{\nu_l} \mathcal{G}_{\lambda}^{\mathrm{t}}(\mathbf{k}, i\nu_l) \mathcal{G}_{\lambda'}^{\mathrm{b}}(\mathbf{k} - \Delta\mathbf{K}_n, i\nu_l + i\omega_n), \tag{A10}$$

with $\langle \lambda, \mathbf{k}|T^{(n)}|\lambda', \mathbf{k} - \Delta\mathbf{K}_n\rangle$ the projection of the tunneling matrices on the eigenstates of band λ and momentum $\mathbf{k}$ of the top graphene layer, and band λ' and momentum $\mathbf{k} - \Delta\mathbf{K}_n$ for the bottom one [cf. Eq. (14)]. Lastly, we perform the Matsubara sum over the fermionic frequency ν_l, perform an analytical continuation, and take the imaginary part to obtain Eq. (10).

The derivation of the spin-dependent tunneling current proceeds in an analogous way. We need to compute

$$
\chi^{(2)}(i\omega_n) = -\int_0^\beta d\tau \, e^{i\omega_n \tau} \langle \mathcal{T} A_2(\tau) A_2^\dagger(0) \rangle
$$

$$
= -\frac{\bar{\Gamma}_1^2}{N} \sum_{\boldsymbol{k},\boldsymbol{k}'} \sum_{n=0}^2 \int_0^\beta d\tau \, e^{i\omega_n \tau} \sum_\gamma \langle \mathcal{T} s^\gamma_{\boldsymbol{k}-\boldsymbol{k}'+\Delta\boldsymbol{K}_n}(\tau) s^\gamma_{-\boldsymbol{k}+\boldsymbol{k}'+\Delta\boldsymbol{K}_n} \rangle \mathrm{Tr}\,[\mathcal{G}^b(\boldsymbol{k}',\tau) T^{(n)} \mathcal{G}^t(\boldsymbol{k},-\tau) T^{(n)}], \tag{A11}
$$

where we assumed that, in the absence of the tunneling Hamiltonian, the quantum spin liquid and graphene layers are uncorrelated. The trace in Eq. (A11) acts again on orbital space and we used that for Pauli matrices $\mathrm{tr}(\sigma^i \sigma^j) = \sum_{s,z} \sigma^i_{sz} \sigma^j_{zs} = \delta_{i,j}$. The Fourier transform to Matsubara frequency space leads to

$$
\chi^{(2)}(i\omega_n) = \sum_{\boldsymbol{q}} \sum_{n=0}^2 \frac{\bar{\Gamma}_1^2}{\beta} \sum_{\Omega_m} \mathcal{G}_s(\boldsymbol{q}+\Delta\boldsymbol{K}_n, i\omega_n + i\Omega_m) \mathcal{G}_{tb}(\boldsymbol{q}, i\Omega_m, n), \tag{A12}
$$

with $\boldsymbol{q} = \boldsymbol{k} - \boldsymbol{k}'$ and

$$
\mathcal{G}_{tb}(\boldsymbol{q}, i\Omega_m, n) = \frac{1}{N} \sum_{\boldsymbol{k},\lambda,\lambda'} |\langle \lambda, \boldsymbol{k} | T^{(n)} | \lambda', \boldsymbol{k}-\boldsymbol{q} \rangle|^2 \frac{1}{\beta} \sum_{\nu_l} \mathcal{G}^t_\lambda(\boldsymbol{k}, i\nu_l) \mathcal{G}^b_{\lambda'}(\boldsymbol{k}-\boldsymbol{q}, i\nu_l - i\Omega_m), \tag{A13}
$$

$$
\mathcal{G}_s(\boldsymbol{q}+\Delta\boldsymbol{K}_n, i\omega_n + i\Omega_m) = -\int_0^\beta d\tau \, e^{i(\omega_n + \Omega_m)\tau} \langle \mathcal{T} s^\gamma_{\boldsymbol{k}-\boldsymbol{k}'+\Delta\boldsymbol{K}_n}(\tau) s^\gamma_{-\boldsymbol{k}+\boldsymbol{k}'+\Delta\boldsymbol{K}_n} \rangle. \tag{A14}
$$

Lastly, we perform the Matsubara sums, perform an analytical continuation, and take the imaginary part to obtain Eq. (11).

In all generality, one would be an additional contribution to the total current linear in $\bar{\Gamma}_1$. This additional term, however, vanishes for spin-nonpolarized leads as it is proportional to $\langle s \rangle$. This last term is given by

$$
\chi^{(1)}(i\omega_n) = -\int_0^\beta d\tau \, e^{i\omega_n \tau} \langle \mathcal{T} A_2(\tau) A_0^\dagger(0) \rangle
$$

$$
= -\frac{\bar{\Gamma}_0 \bar{\Gamma}_1}{N} \sum_\gamma \sum_{\boldsymbol{k},\boldsymbol{q}} \sum_{n,s} \sigma^\gamma_{ss} \langle \mathcal{T} s^\gamma_{\boldsymbol{q}+\Delta\boldsymbol{K}_n}(\tau) \rangle \mathrm{Tr}\,[\mathcal{G}^b(\boldsymbol{k}+\Delta\boldsymbol{K}_n, \tau) T^{(n)} \mathcal{G}^t(\boldsymbol{k}, -\tau) T^{(n)}]. \tag{A15}
$$

In the absence of spin polarization in the leads, the term $\sum_s \sigma^\gamma_{ss}$ results in a vanishing contribution.

APPENDIX B: CONTRIBUTION OF THE ELASTIC TUNNELING TO THE TOTAL CURRENT

We here derive the contribution to the total current stemming from elastic tunneling. We restrict ourselves to the limit $\mu > eV_{tb}$ and consider electron-doped graphene layers. Therefore, we consider tunneling events involving only the conduction bands of the two layers, i.e., $\lambda = \lambda' = +1$. First, from Eq. (14), we note that

$$
\left| T^{(n)}_{+1,+1} \right|^2 = \left[1 + \cos\left(\frac{2\pi n}{3} + \phi_{\boldsymbol{k}} \right) \right] \left[1 + \cos\left(\frac{2\pi n}{3} + \phi_{\boldsymbol{k}-\boldsymbol{q}} \right) \right]. \tag{B1}
$$

We then have

$$
I^{(0)}_{T=0}(eV_{tb}) = -\frac{\sqrt{3}ea_g^2 \bar{\Gamma}_0^2}{2\pi \hbar} \sum_n \int_0^{eV_{tb}} d\epsilon \int d^2\boldsymbol{k} \left[1 + \cos\left(\frac{2\pi n}{3} + \phi_{\boldsymbol{k}} \right) \right] \left[1 + \cos\left(\frac{2\pi n}{3} + \phi_{\boldsymbol{k}-\Delta\boldsymbol{K}_n} \right) \right]
$$

$$
\times \delta(\epsilon - eV_{tb} - \hbar v_F |\boldsymbol{k}| + \mu) \delta(\epsilon - \hbar v_F |\boldsymbol{k} - \Delta\boldsymbol{K}_n| + \mu)
$$

$$
= -\frac{\sqrt{3}ea_g^2 \bar{\Gamma}_0^2}{2\pi \hbar^2 v_F} \sum_n \int d^2\boldsymbol{k} \left[1 + \cos\left(\frac{2\pi n}{3} + \phi_{\boldsymbol{k}} \right) \right] \left[1 + \cos\left(\frac{2\pi n}{3} + \phi_{\boldsymbol{k}-\Delta\boldsymbol{K}_n} \right) \right]
$$

$$
\times \delta\left(\frac{eV_{tb}}{\hbar v_F} + |\boldsymbol{k}| - |\boldsymbol{k} - \Delta\boldsymbol{K}_n| \right) \Theta(eV_{tb} - \hbar v_F |\boldsymbol{k} - \Delta\boldsymbol{K}_n| + \mu), \tag{B2}
$$

where we converted the sum over $\boldsymbol{k}$ in an integral. To perform the integral, we introduce the new variable $p = |\boldsymbol{k} - \Delta\boldsymbol{K}_n|$ and replace the integral over $\phi_{\boldsymbol{k}}$ in $\int d^2\boldsymbol{k} = \int_0^\infty dk \, k \int_0^{2\pi} d\phi_{\boldsymbol{k}}$ via [97]

$$
\int d^2\boldsymbol{k} = \int_0^\infty dk \int_0^{2\pi} d\phi_{\boldsymbol{k}} \int_0^\infty dp \, \frac{p}{\Delta K_n} \delta\left(\frac{p^2 - \Delta K_n^2 - k^2}{2k \Delta K_n} + \cos\phi_{\boldsymbol{k}} \right). \tag{B3}
$$

We also express the cosine and sine of the angles ϕ_k and $\phi_{k+\Delta K_n}$ in Eq. (B1) in terms of the new variables k and p:

$$\cos\phi_k = \frac{\Delta K_n^2 + k^2 - p^2}{2\Delta K_n k}, \tag{B4}$$

$$\cos\phi_{k-\Delta K_n} = \frac{k^2 - \Delta K_n^2 - p^2}{2\Delta K_n p}, \tag{B5}$$

$$\sin\phi_k = \frac{\sqrt{4\Delta K_n^2 k^2 - \left(\Delta K_n^2 + k^2 - p^2\right)^2}}{2\Delta K_n k}, \tag{B6}$$

$$\sin\phi_{k-\Delta K_n} = \frac{\sqrt{4\Delta K_n^2 p^2 - \left(k^2 - \Delta K_n^2 - p^2\right)^2}}{2\Delta K_n p}. \tag{B7}$$

We can now carry out the integral over ϕ_k:

$$
\begin{aligned}
\int_0^{2\pi} \mathrm{d}\phi_k\, \delta\left(\frac{p^2 - \Delta K_n^2 - k^2}{2k\Delta K_n} + \cos\phi_k\right) &= \frac{1}{2\pi}\int_{-\infty}^{+\infty}\mathrm{d}x\int_0^{2\pi}\mathrm{d}\phi_k\, e^{\mathrm{i}x(\frac{p^2-\Delta K_n^2-k^2}{2k\Delta K_n}+\cos\phi_k)} \\
&= \int_{-\infty}^{+\infty}\mathrm{d}x\, e^{\mathrm{i}x\frac{p^2-\Delta K_n^2-k^2}{2k\Delta K_n}} J_0(|x|) \\
&= \frac{4k\Delta K_n}{\sqrt{\left[(p+k)^2 - \Delta K_n^2\right]\left[\Delta K_n^2 - (p-k)^2\right]}},
\end{aligned}
\tag{B8}
$$

where $J_0(x)$ is the zero Bessel's function of the first kind.

With these replacements, and carrying out the sum over n, we obtain

$$
\begin{aligned}
I_{T=0}^{(0)}(eV_{\mathrm{tb}}) = &-\frac{3\sqrt{3}ea_g^2\bar{\Gamma}_0^2}{2\pi\,\hbar^2 v_{\mathrm{F}}}\int_0^\infty \mathrm{d}k\int_0^\infty \mathrm{d}p\,\delta\left(\frac{eV_{\mathrm{tb}}}{\hbar v_{\mathrm{F}}} + k - p\right)\Theta(eV_{\mathrm{tb}} - \hbar v_{\mathrm{F}}p + \mu) \\
&\times \frac{4kp}{\sqrt{\left[(k+p)^2 - \Delta K_n^2\right]\left[\Delta K_n^2 - (p-k)^2\right]}}\left\{1 + \frac{k^2 + p^2 - \Delta K_n^2}{4pk}\right\}.
\end{aligned}
\tag{B9}
$$

The remaining integrals can now be readily solved to obtain

$$
\begin{aligned}
I_{T=0}^{(0)}(eV_{\mathrm{tb}}) = &-\frac{3\sqrt{3}ea_g^2\bar{\Gamma}_0^2}{16\pi\,\hbar^3 v_{\mathrm{F}}^2\sqrt{\hbar^2 v_{\mathrm{F}}^2\Delta K_n^2 - eV_{\mathrm{tb}}^2}}\Theta[\hbar v_{\mathrm{F}}\Delta K_n - eV_{\mathrm{tb}}]\Theta[eV_{\mathrm{tb}} + 2\mu - \hbar v_{\mathrm{F}}\Delta K_n] \\
&\times \left[3(eV_{\mathrm{tb}} + 2\mu)\sqrt{(eV_{\mathrm{tb}} + 2\mu)^2 - \hbar^2 v_{\mathrm{F}}^2\Delta K_n^2}\right. \\
&\left. - (\hbar^2 v_{\mathrm{F}}^2\Delta K_n^2 + 2eV_{\mathrm{tb}}^2)\log\left(\frac{eV_{\mathrm{tb}} + 2\mu}{\hbar v_{\mathrm{F}}\Delta K_n} + \sqrt{\frac{(eV_{\mathrm{tb}} + 2\mu)^2}{\hbar^2 v_{\mathrm{F}}^2\Delta K_n^2} - 1}\right)\right].
\end{aligned}
\tag{B10}
$$

As stressed in the main text, the elastic tunneling contributes to the total current, and hence to the IETS signal, only if $eV_{\mathrm{tb}} < \hbar v_{\mathrm{F}}|\Delta K_n| < eV_{\mathrm{tb}} + 2\mu$.

APPENDIX C: DERIVATION OF THE SPIN STRUCTURE FACTOR

As discussed in Sec. IV, we represent the physical spins in terms of Abrikosov fermions. We choose fermions rather than Schwinger bosons as they allow us to easily treat gapless quantum spin liquid without worrying about the condensation of the spinons. We define

$$s(r) = \frac{1}{2}\sum_{s,s'} f_{r,s}^\dagger \boldsymbol{\sigma}_{ss'} f_{r\beta}, \tag{C1}$$

where $f_{r,s}$ annihilates a spinon at location r with spin s. Imposing constraints to avoid unphysical states, such as empty or doubly occupied sites, i.e., $\sum_s f_{rs}^\dagger f_{rs} = 1$ and $f_{is}f_{is'}\epsilon_{ss'} = 0$, introduces additional gauge degrees of freedom. At the mean-field level, we neglect gauge fluctuations and enforce the constraints only on average. By introducing auxiliary fields to decouple the quartic term in the spinon operators, we obtain the quadratic Hamiltonian for the spinons that serves as the basis for further analysis:

$$H_{\mathrm{QSL}} = \sum_{r_i r_j, ss'}\left(t_{r_i r_j} f_{is}^\dagger f_{js} + \Delta_{r_i r_j} f_{is}^\dagger f_{js'}^\dagger + \mathrm{H.c.}\right). \tag{C2}$$

Here, $\Delta \neq 0$ describes a $\mathbb{Z}_2$ QSL, whereas, a U(1) QSL requires $\Delta = 0$. The chemical potential, included in $t_{\boldsymbol{r}_i \boldsymbol{r}_j}$, enforces the half-filling condition of the spinon bands.

We now derive the spin structure factor expressed in terms of the spinon operators, as shown in Eq. (19). We will consider the possibility of multiple sublattices in the unit cell at locations $\boldsymbol{r}_i = \boldsymbol{R}_i + \boldsymbol{\delta}_\alpha$, where $\boldsymbol{R}_i$ is the unit-cell center and $\boldsymbol{\delta}_\alpha$ the position of the sublattice inside the unit cell:

$$
\begin{aligned}
\mathcal{G}_s(\boldsymbol{q}, i\omega_n) &= \frac{1}{N} \sum_\gamma \sum_{\alpha,\beta} \int_0^\beta d\tau \, e^{i\tau\omega_n} \sum_{ij} e^{i\boldsymbol{q}\cdot(\boldsymbol{r}_i - \boldsymbol{r}_j)} \langle \mathcal{T} s_{i\alpha}^\gamma(\tau) s_{j\beta}^\gamma \rangle \\
&= \frac{1}{4N} \sum_\gamma \sum_{\substack{ss' \\ zz'}} \sum_{\alpha,\beta} \sigma_{ss'}^\gamma \sigma_{zz'}^\gamma \int_0^\beta d\tau \, e^{i\tau\omega_n} \sum_{ij} e^{i\boldsymbol{q}\cdot(\boldsymbol{r}_i - \boldsymbol{r}_j)} \langle \mathcal{T} f_{\alpha i s}^\dagger(\tau) f_{\alpha i s'}(\tau) f_{\beta j z}^\dagger f_{\beta j z'} \rangle \\
&= \frac{1}{4N} \sum_{ss'} \sum_{\alpha,\beta} \int_0^\beta d\tau \, e^{i\tau\omega_n} \sum_{ij} e^{i\boldsymbol{q}\cdot(\boldsymbol{r}_i - \boldsymbol{r}_j)} [2\langle \mathcal{T} f_{\alpha i s}^\dagger(\tau) f_{\alpha i s'}(\tau) f_{\beta j s'}^\dagger f_{\beta j s} \rangle - \langle \mathcal{T} f_{\alpha i s}^\dagger(\tau) f_{\alpha i s}(\tau) f_{\beta j s'}^\dagger f_{\beta j s'} \rangle] \\
&= \frac{1}{4N} \sum_{\boldsymbol{k}\boldsymbol{k}'} \sum_{ss'} \sum_{\alpha,\beta} \int_0^\beta d\tau \, e^{i\tau\omega_n} e^{i\boldsymbol{q}\cdot(\boldsymbol{\delta}_\alpha - \boldsymbol{\delta}_\beta)} [2\langle \mathcal{T} f_{\alpha \boldsymbol{k} s}^\dagger(\tau) f_{\alpha \boldsymbol{k}+\boldsymbol{q} s'}(\tau) f_{\beta \boldsymbol{k}' s'}^\dagger f_{\beta \boldsymbol{k}'-\boldsymbol{q} s} \rangle - \langle \mathcal{T} f_{\alpha \boldsymbol{k} s}^\dagger(\tau) f_{\alpha \boldsymbol{k}+\boldsymbol{q} s}(\tau) f_{\beta \boldsymbol{k}' s'}^\dagger f_{\beta \boldsymbol{k}'-\boldsymbol{q} s'} \rangle],
\end{aligned}
$$

(C3)

where, in the second line, we used that $\sum_\gamma \sigma_{ss'}^\gamma \sigma_{zz'}^\gamma = 2\delta_{s,z'}\delta_{z,s'} - \delta_{s,s'}\delta_{z,z'}$.

We restrict ourselves to the case of a U(1) quantum spin liquid. As a first step, we move from orbital to band basis:

$$
f_{n\boldsymbol{k}s} = \sum_\alpha U_{\alpha n s} f_{\alpha \boldsymbol{k}s},
$$

(C4)

where $U_{\alpha n s}$ is the nth eigenvector of the spinon mean-field Hamiltonian at momentum $\boldsymbol{k}$ with spin s at sublattice α:

$$
\begin{aligned}
\mathcal{G}_s(\boldsymbol{q}, i\omega_n) &= \frac{1}{4N} \sum_{\boldsymbol{k}\boldsymbol{k}'} \sum_{\alpha\beta} \sum_{s,s'} \sum_{nlqt} \int_0^\beta d\tau \, e^{i\tau\omega_n} e^{i\boldsymbol{q}\cdot(\boldsymbol{\delta}_\alpha - \boldsymbol{\delta}_\beta)} \\
&\quad \times [2 U_{\alpha n s}^*(\boldsymbol{k}) U_{\alpha l s'}(\boldsymbol{k}+\boldsymbol{q}) U_{\beta q s'}^*(\boldsymbol{k}') U_{\beta t s}(\boldsymbol{k}'-\boldsymbol{q}) \langle \mathcal{T} f_{n\boldsymbol{k}s}^\dagger(\tau) f_{l\boldsymbol{k}+\boldsymbol{q}s'}(\tau) f_{q\boldsymbol{k}'s'}^\dagger f_{t\boldsymbol{k}'-\boldsymbol{q}s} \rangle \\
&\quad - U_{\alpha n s}^*(\boldsymbol{k}) U_{\alpha l s}(\boldsymbol{k}+\boldsymbol{q}) U_{\beta q s'}^*(\boldsymbol{k}') U_{\beta t s'}(\boldsymbol{k}'-\boldsymbol{q}) \langle \mathcal{T} f_{n\boldsymbol{k}s}^\dagger(\tau) f_{l\boldsymbol{k}+\boldsymbol{q}s}(\tau) f_{q\boldsymbol{k}'s'}^\dagger f_{t\boldsymbol{k}'-\boldsymbol{q}s'} \rangle] \\
&= \frac{1}{4N} \sum_{\boldsymbol{k}\boldsymbol{k}'} \sum_{\alpha\beta} \sum_{s,s'} \sum_{nlqt} \int_0^\beta d\tau \, e^{i\tau\omega_n} e^{i\boldsymbol{q}\cdot(\boldsymbol{\delta}_\alpha - \boldsymbol{\delta}_\beta)} U_{\alpha n s}^*(\boldsymbol{k}) U_{\alpha l s'}(\boldsymbol{k}+\boldsymbol{q}) U_{\beta q s'}^*(\boldsymbol{k}') U_{\beta t s}(\boldsymbol{k}'-\boldsymbol{q}) \\
&\quad \times [2 G_{ss}^n(\boldsymbol{k}, -\tau) G_{s's'}^l(\boldsymbol{k}+\boldsymbol{q}, \tau) \delta_{nt} \delta_{lq} \delta_{\boldsymbol{k},\boldsymbol{k}'-\boldsymbol{q}} - G_{ss}^n(\boldsymbol{k}, -\tau) G_{s's'}^l(\boldsymbol{k}+\boldsymbol{q}, \tau) \delta_{ss'} \delta_{nt} \delta_{lq} \delta_{\boldsymbol{k},\boldsymbol{k}'-\boldsymbol{q}}] \\
&= \frac{1}{4N} \sum_{\boldsymbol{k}} \sum_{ss'} \sum_{nl} \int_0^\beta d\tau \, e^{i\tau\omega_n} g_{ss'}(\boldsymbol{k}, \boldsymbol{q}, n, l)(2 - \delta_{ss'}) G_{ss}^n(\boldsymbol{k}, -\tau) G_{s's'}^l(\boldsymbol{k}+\boldsymbol{q}, \tau).
\end{aligned}
$$

(C5)

We introduced the spinons Green's functions

$$
\begin{aligned}
G_{ss}^n(\boldsymbol{k}, \tau) &= \langle \mathcal{T} f_{ns\boldsymbol{k}}(\tau) f_{ns\boldsymbol{k}}^\dagger \rangle, \\
G_{ss}^n(\boldsymbol{k}, -\tau) &= \langle \mathcal{T} f_{ns\boldsymbol{k}}^\dagger(\tau) f_{ns\boldsymbol{k}} \rangle,
\end{aligned}
$$

(C6)

and the function g that accounts for the overlap of the eigenstates' wave functions:

$$
g_{ss'}(\boldsymbol{k}, \boldsymbol{q}, n, l) = \left| \sum_\alpha e^{i\boldsymbol{q}\cdot\boldsymbol{\delta}_\alpha} U_{\alpha n s}^*(\boldsymbol{k}) U_{\alpha l s'}(\boldsymbol{k}+\boldsymbol{q}) \right|^2.
$$

(C7)

With the fermionic Matsubara frequencies ν_l and Ω_l, we can rewrite the spinon Green's function in frequency space:

$$
\begin{aligned}
G_{ss}^n(\boldsymbol{k}+\boldsymbol{q}, \tau) &= \frac{1}{\beta} \sum_{\Omega_l} e^{i\Omega_l \tau} G_{ss}^n(\boldsymbol{k}+\boldsymbol{q}, i\Omega_l), \\
G_{ss}^n(\boldsymbol{k}, -\tau) &= \frac{1}{\beta} \sum_{\nu_l} e^{-i\nu_l \tau} G_{ss}^n(\boldsymbol{k}, i\nu_l).
\end{aligned}
$$

(C8)

We then obtain

$$\mathcal{G}_s(\boldsymbol{q}, i\omega_n) = \frac{1}{4N} \sum_{\boldsymbol{k}} \sum_{ss'} \sum_{nl} \frac{1}{\beta} \sum_{\Omega_l} g_{ss'}(\boldsymbol{k}, \boldsymbol{q}, n, l)(2 - \delta_{ss'}) G_{ss}^n(\boldsymbol{k}, i\Omega_l + i\omega_n) G_{s's'}^l(\boldsymbol{k} + \boldsymbol{q}, i\Omega_l). \tag{C9}$$

Note that $i\omega_n = i\nu_l - i\Omega_l$ is a bosonic Matsubara frequency. We can finally perform the Matsubara sum over Ω_l and obtain

$$\mathcal{G}_s(\boldsymbol{q}, i\omega_n) = -\frac{1}{4N} \sum_{ss'} \sum_{\boldsymbol{k}} \sum_{nl} g_{ss'}(\boldsymbol{k}, \boldsymbol{q}, n, l)(2 - \delta_{ss'}) \frac{n_F(\xi_{n\boldsymbol{k}}^s) - n_F(\xi_{l\boldsymbol{k}+\boldsymbol{q}}^{s'})}{i\omega_n - \xi_{n\boldsymbol{k}}^s + \xi_{l\boldsymbol{k}+\boldsymbol{q}}^{s'}}. \tag{C10}$$

Finally, performing an analytical continuation and taking the imaginary part, we reach

$$S(\boldsymbol{q}, \omega) = \frac{1}{4N} \sum_{ss'} \sum_{\boldsymbol{k}} \sum_{nl} g_{ss'}(\boldsymbol{k}, \boldsymbol{q}, n, l)(2 - \delta_{ss'}) \big[n_F(\xi_{n\boldsymbol{k}}^s) - n_F(\xi_{l\boldsymbol{k}+\boldsymbol{q}}^{s'}) \big] \delta\big(\omega - \xi_{n\boldsymbol{k}}^s + \xi_{l\boldsymbol{k}+\boldsymbol{q}}^{s'}\big), \tag{C11}$$

which corresponds to Eq. (19).

1. Dirac quantum spin liquid

We can first study a gapless U(1) quantum spin liquid where spinons have a massless Dirac dispersion: a Dirac quantum spin liquid. The low-energy dispersion is given by $\xi_{n\boldsymbol{k}} = \hbar v_s n |\boldsymbol{k}|$, with $n = \pm$ and v_s the spinon Fermi velocity.

The computation of spin structure factor of a Dirac quantum spin liquid is analogous to the derivation of the particle-hole spectral function of graphene presented in Appendix B, without the additional complication of the scattering matrix of the graphene bilayer's structure.

We readily obtain

$$S(\boldsymbol{q}, \omega) = \frac{3\Omega}{2} \int \frac{d^2\boldsymbol{k}}{(2\pi)^2} \delta(\omega - \hbar v_s |\boldsymbol{k}| - \hbar v_s |\boldsymbol{k} + \boldsymbol{q}|) = \frac{3\Omega}{16\pi \hbar^2 v_s^2} \frac{\omega^2 - \hbar^2 v_s^2 q^2/2}{\sqrt{\omega^2 - \hbar^2 v_s^2 q^2}} \Theta(\omega - \hbar v_s q), \tag{C12}$$

where Ω is the area of the QSL's unit cell.

2. Chiral quantum spin liquid

To capture a U(1) chiral spin liquid, we consider a spinon model with a gap in the spectrum. For simplicity, we assume that the spinon dispersion has a minimum at $\boldsymbol{k} = 0$ for the conduction band and a maximum at the same location for the valence band. The gap at $\boldsymbol{k} = 0$ is Δ_s. We consider the dispersion $\xi_{n\boldsymbol{k}} = n(\frac{\hbar^2 k^2}{2m_s} + \frac{\Delta_s}{2})$, with $n = \pm$ and m_s the spinon mass. At zero temperature, we need to consider exclusively transition from the valence to the conduction band, i.e., $n = +$ and $l = -$ in Eq. (C11).

The integral to compute is

$$S(\boldsymbol{q}, \omega) = \frac{3\Omega}{2} \int \frac{d^2\boldsymbol{k}}{(2\pi)^2} \delta\left(\omega - \Delta_s - \frac{\hbar^2 k^2}{2m_s} - \frac{\hbar^2 (\boldsymbol{k} + \boldsymbol{q})^2}{2m_s}\right). \tag{C13}$$

It can be readily solved:

$$\begin{aligned}
S(\boldsymbol{q}, \omega) &= \frac{3\Omega}{2} \int \frac{d^2\boldsymbol{k}}{(2\pi)^2} \delta\left(\omega - \Delta - \frac{\hbar^2 k^2}{m_s} - \frac{\hbar^2 q^2}{2m_s} - \frac{\hbar^2 kq \cos\phi_{\boldsymbol{k}}}{m_s}\right) \\
&= \frac{3\Omega}{2} \int \frac{d^2\boldsymbol{k}}{(2\pi)^2} \delta\left(\omega - \Delta - \frac{\hbar^2 q^2}{4m_s} - \frac{\hbar^2 (\boldsymbol{k} - \boldsymbol{q}/2)^2}{m_s}\right) \\
&= \frac{3m_s\Omega}{8\pi^2} \int_0^\infty dp \int_0^{2\pi} d\phi_{\boldsymbol{p}}\, p\, \delta\left[m_s\left(\omega - \Delta - \frac{\hbar^2 q^2}{4m_s}\right) - \hbar^2 p^2\right] \\
&= \frac{3m_s\Omega}{8\pi \hbar^2} \Theta\left(\omega - \Delta - \frac{\hbar^2 q^2}{4m_s}\right).
\end{aligned} \tag{C14}$$

A completely analogous result captures the zero-temperature low-energy and small-momentum spin structure factor of a gapped $\mathbb{Z}_2$ spin liquid.

3. Spinon Fermi surface

The calculation of the spin structure factor in the presence of a spinon Fermi surface is analogous to the calculation of the dynamical spin structure factor of a neutral Fermi gas [79].

For the spinons, we assume a simple parabolic dispersion with mass m_s and Fermi momentum $k_{s,F}$. If we restrict to small momentum $\boldsymbol{q}$, the states contributing to the dynamical spin structure factor $\mathcal{S}(\boldsymbol{q}, \omega)$ are those in the crescent defined by $|\boldsymbol{k}| < k_{s,F}$ and $|\boldsymbol{k} + \boldsymbol{q}| > k_{s,F}$. We have

$$
\begin{aligned}
\mathcal{S}(\boldsymbol{q}, \omega) &= \frac{3}{2} \frac{1}{2 k_{s,F} q} \int_{\substack{k < k_{s,F} \\ |\boldsymbol{k}+\boldsymbol{q}| > k_{s,F}}} \frac{\mathrm{d}^2 \boldsymbol{k}}{(2\pi)^2} \delta\left(\omega + \frac{\hbar^2 k^2}{2 m_s} - \frac{\hbar^2 (\boldsymbol{k}+\boldsymbol{q})^2}{2 m_s} \right) \\
&= \frac{3}{2} \frac{1}{2 k_{s,F} q} \int_{\substack{k < k_{s,F} \\ |\boldsymbol{k}+\boldsymbol{q}| > k_{s,F}}} \frac{\mathrm{d}^2 \boldsymbol{k}}{(2\pi)^2} \delta\left(\omega - \frac{\hbar^2 q^2}{2 m_s} - \frac{\hbar^2 q k \cos \phi_k}{m_s} \right),
\end{aligned}
\tag{C15}
$$

where ϕ_k is the angle between $\boldsymbol{k}$ and $\boldsymbol{q}$.

For small $\boldsymbol{q}$, we can express the number of states in the crescent between ϕ_k and $\phi_k + \mathrm{d}\phi_k$ as

$$
\frac{\mathrm{d}^2 \boldsymbol{k}}{(2\pi^2)} = \frac{k_{s,F} q \, \cos \phi_k \, \mathrm{d}\phi_k}{(2\pi)^2},
\tag{C16}
$$

where we approximated $\mathrm{d}k = q \cos \phi_k$. We finally obtain

$$
\begin{aligned}
\mathcal{S}(\boldsymbol{q}, \omega) &= \frac{3}{16 \pi^2 \hbar q v_s} \int_{-\pi/2}^{\pi/2} \mathrm{d}\phi_k \cos \phi_k \, \delta\left(\frac{\omega}{\hbar q v_s} - \cos \phi_k \right) \\
&= \frac{3}{8 \pi^2 \hbar q v_s} \frac{\omega}{\sqrt{\hbar^2 q^2 v_s^2 - \omega^2}} \Theta(\hbar q v_s - \omega),
\end{aligned}
\tag{C17}
$$

where the Fermi velocity is defined as $v_s = \hbar k_{s,F} / m_s$, and we neglected the contribution $\hbar^2 q^2 / 2 m_s$ in the delta function. This expression corresponds to Eq. (23) of the main text.

[1] X.-G. Wen, Quantum orders and symmetric spin liquids, Phys. Rev. B **65**, 165113 (2002).

[2] Y. Zhou, K. Kanoda, and T.-K. Ng, Quantum spin liquid states, Rev. Mod. Phys. **89**, 025003 (2017).

[3] L. Savary and L. Balents, Quantum spin liquids: a review, Rep. Prog. Phys. **80**, 016502 (2017).

[4] J. Knolle and R. Moessner, A field guide to spin liquids, Annu. Rev. Condens. Matter Phys. **10**, 451 (2019).

[5] J. Wen, S.-L. Yu, S. Li, W. Yu, and J.-X. Li, Experimental identification of quantum spin liquids, npj Quantum Mater. **4**, 12 (2019).

[6] C. Broholm, R. J. Cava, S. A. Kivelson, D. G. Nocera, M. R. Norman, and T. Senthil, Quantum spin liquids, Science **367**, eaay0668 (2020).

[7] I. A. Leahy, C. A. Pocs, P. E. Siegfried, D. Graf, S.-H. Do, K.-Y. Choi, B. Normand, and M. Lee, Anomalous thermal conductivity and magnetic torque response in the honeycomb magnet α-RuCl$_3$, Phys. Rev. Lett. **118**, 187203 (2017).

[8] D. Watanabe, K. Sugii, M. Shimozawa, Y. Suzuki, T. Yajima, H. Ishikawa, Z. Hiroi, T. Shibauchi, Y. Matsuda, and M. Yamashita, Emergence of nontrivial magnetic excitations in a spin-liquid state of kagomé volborthite, Proc. Natl. Acad. Sci. USA **113**, 8653 (2016).

[9] M. Yamashita, N. Nakata, Y. Kasahara, T. Sasaki, N. Yoneyama, N. Kobayashi, S. Fujimoto, T. Shibauchi, and Y. Matsuda, Thermal-transport measurements in a quantum spin-liquid state of the frustrated triangular magnet κ-(BEDT-TTF)$_2$Cu$_2$(CN)$_3$, Nat. Phys. **5**, 44 (2009).

[10] M. Yamashita, N. Nakata, Y. Senshu, M. Nagata, H. M. Yamamoto, R. Kato, T. Shibauchi, and Y. Matsuda, Highly mobile gapless excitations in a two-dimensional candidate quantum spin liquid, Science **328**, 1246 (2010).

[11] M. Mączka, M. L. Sanjuán, A. F. Fuentes, K. Hermanowicz, and J. Hanuza, Temperature-dependent Raman study of the spin-liquid pyrochlore Tb$_2$Ti$_2$O$_7$, Phys. Rev. B **78**, 134420 (2008).

[12] D. Wulferding, P. Lemmens, P. Scheib, J. Röder, P. Mendels, S. Chu, T. Han, and Y. S. Lee, Interplay of thermal and quantum spin fluctuations in the kagome lattice compound herbertsmithite, Phys. Rev. B **82**, 144412 (2010).

[13] A. Little, L. Wu, P. Lampen-Kelley, A. Banerjee, S. Patankar, D. Rees, C. A. Bridges, J.-Q. Yan, D. Mandrus, S. E. Nagler, and J. Orenstein, Antiferromagnetic resonance and terahertz continuum in α-RuCl$_3$, Phys. Rev. Lett. **119**, 227201 (2017).

[14] Z. Wang, S. Reschke, D. Hüvonen, S.-H. Do, K.-Y. Choi, M. Gensch, U. Nagel, T. Room, and A. Loidl, Magnetic excitations and continuum of a possibly field-induced quantum spin liquid in α-RuCl$_3$, Phys. Rev. Lett. **119**, 227202 (2017).

[15] C. Wellm, J. Zeisner, A. Alfonsov, A. U. B. Wolter, M. Roslova, A. Isaeva, T. Doert, M. Vojta, B. Büchner, and V. Kataev, Signatures of low-energy fractionalized excitations in α-RuCl$_3$ from field-dependent microwave absorption, Phys. Rev. B **98**, 184408 (2018).

[16] L. J. Sandilands, Y. Tian, K. W. Plumb, Y.-J. Kim, and K. S. Burch, Scattering continuum and possible fractionalized excitations in α-RuCl$_3$, Phys. Rev. Lett. **114**, 147201 (2015).

[17] A. Yaouanc and P. de Réotier, *Muon Spin Rotation, Relaxation, and Resonance: Applications to Condensed Matter*, International Series of Monographs on Physics (Oxford University Press, Oxford, 2010).

[18] P. Carretta and A. Keren, Nmr and μsr in highly frustrated magnets, in *Introduction to Frustrated Magnetism: Materials,*

Experiments, Theory, edited by C. Lacroix, P. Mendels, and F. Mila (Springer, Berlin, 2011), pp. 79–105.

[19] S. Chatterjee and S. Sachdev, Probing excitations in insulators via injection of spin currents, Phys. Rev. B **92**, 165113 (2015).

[20] C.-Z. Chen, Q.-F. Sun, F. Wang, and X. C. Xie, Detection of spinons via spin transport, Phys. Rev. B **88**, 041405(R) (2013).

[21] S. Chatterjee, J. F. Rodriguez-Nieva, and E. Demler, Diagnosing phases of magnetic insulators via noise magnetometry with spin qubits, Phys. Rev. B **99**, 104425 (2019).

[22] J. Y. Khoo, F. Pientka, P. A. Lee, and I. S. Villadiego, Probing the quantum noise of the spinon Fermi surface with NV centers, Phys. Rev. B **106**, 115108 (2022).

[23] P. A. Lee and S. Morampudi, Proposal to detect emergent gauge field and its Meissner effect in spin liquids using NV centers, Phys. Rev. B **107**, 195102 (2023).

[24] D. F. Mross and T. Senthil, Charge Friedel oscillations in a Mott insulator, Phys. Rev. B **84**, 041102(R) (2011).

[25] S. C. Morampudi, A. M. Turner, F. Pollmann, and F. Wilczek, Statistics of fractionalized excitations through threshold spectroscopy, Phys. Rev. Lett. **118**, 227201 (2017).

[26] G. Chen and J. L. Lado, Impurity-induced resonant spinon zero modes in Dirac quantum spin liquids, Phys. Rev. Res. **2**, 033466 (2020).

[27] M. R. Norman and T. Micklitz, How to measure a spinon Fermi surface, Phys. Rev. Lett. **102**, 067204 (2009).

[28] J. Aftergood and S. Takei, Probing quantum spin liquids in equilibrium using the inverse spin Hall effect, Phys. Rev. Res. **2**, 033439 (2020).

[29] R. Mazzilli, A. Levchenko, and E. J. König, Drag resistance mediated by quantum spin liquids, Phys. Rev. B **108**, 014425 (2023).

[30] T.-H. Han, J. S. Helton, S. Chu, D. G. Nocera, J. A. Rodriguez-Rivera, C. Broholm, and Y. S. Lee, Fractionalized excitations in the spin-liquid state of a kagome-lattice antiferromagnet, Nature (London) **492**, 406 (2012).

[31] B. Lake, D. A. Tennant, J.-S. Caux, T. Barthel, U. Schollwöck, S. E. Nagler, and C. D. Frost, Multispinon continua at zero and finite temperature in a near-ideal Heisenberg chain, Phys. Rev. Lett. **111**, 137205 (2013).

[32] M. Mourigal, M. Enderle, A. Klöpperpieper, J.-S. Caux, A. Stunault, and H. M. Rønnow, Fractional spinon excitations in the quantum Heisenberg antiferromagnetic chain, Nat. Phys. **9**, 435 (2013).

[33] A. Banerjee, J. Yan, J. Knolle, C. A. Bridges, M. B. Stone, M. D. Lumsden, D. G. Mandrus, D. A. Tennant, R. Moessner, and S. E. Nagler, Neutron scattering in the proximate quantum spin liquid α-RuCl₃, Science **356**, 1055 (2017).

[34] J. A. Paddison, M. Daum, Z. Dun, G. Ehlers, Y. Liu, M. B. Stone, H. Zhou, and M. Mourigal, Continuous excitations of the triangular-lattice quantum spin liquid YbMgGaO₄, Nat. Phys. **13**, 117 (2017).

[35] A. Banerjee, C. Bridges, J.-Q. Yan, A. Aczel, L. Li, M. Stone, G. Granroth, M. Lumsden, Y. Yiu, J. Knolle *et al.*, Proximate Kitaev quantum spin liquid behaviour in a honeycomb magnet, Nat. Mater. **15**, 733 (2016).

[36] K. S. Novoselov, D. Jiang, F. Schedin, T. J. Booth, V. V. Khotkevich, S. V. Morozov, and A. K. Geim, Two-dimensional atomic crystals, Proc. Natl. Acad. Sci. USA **102**, 10451 (2005).

[37] A. Inbar, J. Birkbeck, J. Xiao, T. Taniguchi, K. Watanabe, B. Yan, Y. Oreg, A. Stern, E. Berg, and S. Ilani, The quantum twisting microscope, Nature (London) **614**, 682 (2023).

[38] J. Fernández-Rossier, Theory of single-spin inelastic tunneling spectroscopy, Phys. Rev. Lett. **102**, 256802 (2009).

[39] J. Fransson, O. Eriksson, and A. V. Balatsky, Theory of spin-polarized scanning tunneling microscopy applied to local spins, Phys. Rev. B **81**, 115454 (2010).

[40] D. R. Klein, D. MacNeill, J. L. Lado, D. Soriano, E. Navarro-Moratalla, K. Watanabe, T. Taniguchi, S. Manni, P. Canfield, J. Fernández-Rossier, and P. Jarillo-Herrero, Probing magnetism in 2D van der Waals crystalline insulators via electron tunneling, Science **360**, 1218 (2018).

[41] D. Ghazaryan, M. T. Greenaway, Z. Wang, V. H. Guarochico-Moreira, I. J. Vera-Marun, J. Yin, Y. Liao, S. V. Morozov, O. Kristanovski, A. I. Lichtenstein, M. I. Katsnelson, F. Withers, A. Mishchenko, L. Eaves, A. K. Geim, K. S. Novoselov, and A. Misra, Magnon-assisted tunnelling in van der Waals heterostructures based on CrBr₃, Nat. Electron. **1**, 344 (2018).

[42] M. Carrega, I. J. Vera-Marun, and A. Principi, Tunneling spectroscopy as a probe of fractionalization in two-dimensional magnetic heterostructures, Phys. Rev. B **102**, 085412 (2020).

[43] E. J. König, M. T. Randeria, and B. Jäck, Tunneling spectroscopy of quantum spin liquids, Phys. Rev. Lett. **125**, 267206 (2020).

[44] J. Feldmeier, W. Natori, M. Knap, and J. Knolle, Local probes for charge-neutral edge states in two-dimensional quantum magnets, Phys. Rev. B **102**, 134423 (2020).

[45] Y. Chen, W.-Y. He, W. Ruan, J. Hwang, S. Tang, R. L. Lee, M. Wu, T. Zhu, C. Zhang, H. Ryu, F. Wang, S. G. Louie, Z.-X. Shen, S.-K. Mo, P. A. Lee, and M. F. Crommie, Evidence for a spinon Kondo effect in cobalt atoms on single-layer 1T-TaSe₂, Nat. Phys. **18**, 1335 (2022).

[46] W. Ruan, Y. Chen, S. Tang, J. Hwang, H.-Z. Tsai, R. L. Lee, M. Wu, H. Ryu, S. Kahn, F. Liou, C. Jia, A. Aikawa, C. Hwang, F. Wang, Y. Choi, S. G. Louie, P. A. Lee, Z.-X. Shen, S.-K. Mo, and M. F. Crommie, Evidence for quantum spin liquid behaviour in single-layer 1T-TaSe₂ from scanning tunnelling microscopy, Nat. Phys. **17**, 1154 (2021).

[47] W.-Y. He and P. A. Lee, Magnetic impurity as a local probe of the $U(1)$ quantum spin liquid with spinon Fermi surface, Phys. Rev. B **105**, 195156 (2022).

[48] W.-Y. He and P. A. Lee, Electronic density of states of a $U(1)$ quantum spin liquid with spinon Fermi surface. I. Orbital magnetic field effects, Phys. Rev. B **107**, 195155 (2023).

[49] W.-Y. He and P. A. Lee, Electronic density of states of a $U(1)$ quantum spin liquid with spinon Fermi surface. II. Zeeman magnetic field effects, Phys. Rev. B **107**, 195156 (2023).

[50] S.-Q. Jia, L.-J. Zou, Y.-M. Quan, X.-L. Yu, and H.-Q. Lin, Electron tunneling spectroscopy of the anisotropic Kitaev quantum spin liquid sandwiched with superconductors, Phys. Rev. Res. **4**, 023251 (2022).

[51] W.-H. Kao, N. B. Perkins, and G. B. Halász, Vacancy spectroscopy of non-Abelian Kitaev spin liquids, arXiv:2307.10376.

[52] A. Mitra, A. Corticelli, P. Ribeiro, and P. A. McClarty, Magnon interference tunneling spectroscopy as a probe of 2D magnetism, Phys. Rev. Lett. **130**, 066701 (2023).

[53] F. Eickhoff, E. Kolodzeiski, T. Esat, N. Fournier, C. Wagner, T. Deilmann, R. Temirov, M. Rohlfing, F. S. Tautz, and F. B. Anders, Inelastic electron tunneling spectroscopy for probing

strongly correlated many-body systems by scanning tunneling microscopy, Phys. Rev. B **101**, 125405 (2020).

[54] T. Bauer, L. R. D. Freitas, R. G. Pereira, and R. Egger, Scanning tunneling spectroscopy of Majorana zero modes in a Kitaev spin liquid, Phys. Rev. B **107**, 054432 (2023).

[55] R. Bistritzer and A. H. MacDonald, Transport between twisted graphene layers, Phys. Rev. B **81**, 245412 (2010).

[56] A. Mishchenko, J. S. Tu, Y. Cao, R. V. Gorbachev, J. R. Wallbank, M. T. Greenaway, V. E. Morozov, S. V. Morozov, M. J. Zhu, S. L. Wong, F. Withers, C. R. Woods, Y.-J. Kim, K. Watanabe, T. Taniguchi, E. E. Vdovin, O. Makarovsky, T. M. Fromhold, V. I. Fal'ko, A. K. Geim *et al.*, Twist-controlled resonant tunnelling in graphene/boron nitride/graphene heterostructures, Nat. Nanotechnol. **9**, 808 (2014).

[57] K. A. Guerrero-Becerra, A. Tomadin, and M. Polini, Resonant tunneling and the quasiparticle lifetime in graphene/boron nitride/graphene heterostructures, Phys. Rev. B **93**, 125417 (2016).

[58] J. A. Wilson, F. J. Di Salvo, and S. Mahajan, Charge-density waves in metallic, layered, transition-metal dichalcogenides, Phys. Rev. Lett. **32**, 882 (1974).

[59] P. Fazekas and E. Tosatti, Electrical, structural and magnetic properties of pure and doped 1T-TaS$_2$, Philos. Mag., Part B **39**, 229 (1979).

[60] K. T. Law and P. A. Lee, 1T-TaS$_2$ as a quantum spin liquid, Proc. Natl. Acad. Sci. USA **114**, 6996 (2017).

[61] W.-Y. He, X. Y. Xu, G. Chen, K. T. Law, and P. A. Lee, Spinon Fermi surface in a cluster Mott insulator model on a triangular lattice and possible application to 1T-TaS$_2$, Phys. Rev. Lett. **121**, 046401 (2018).

[62] A. Ribak, I. Silber, C. Baines, K. Chashka, Z. Salman, Y. Dagan, and A. Kanigel, Gapless excitations in the ground state of 1T-TaS$_2$, Phys. Rev. B **96**, 195131 (2017).

[63] S. Mañas-Valero, B. M. Huddart, T. Lancaster, E. Coronado, and F. L. Pratt, Quantum phases and spin liquid properties of 1T-TaS$_2$, npj Quantum Mater. **6**, 69 (2021).

[64] Y. J. Yu, Y. Xu, L. P. He, M. Kratochvilova, Y. Y. Huang, J. M. Ni, L. Wang, S.-W. Cheong, J.-G. Park, and S. Y. Li, Heat transport study of the spin liquid candidate 1T-TaS$_2$, Phys. Rev. B **96**, 081111(R) (2017).

[65] T. Ritschel, H. Berger, and J. Geck, Stacking-driven gap formation in layered 1T-TaS$_2$, Phys. Rev. B **98**, 195134 (2018).

[66] Y. D. Wang, W. L. Yao, Z. M. Xin, T. T. Han, Z. G. Wang, L. Chen, C. Cai, Y. Li, and Y. Zhang, Band insulator to Mott insulator transition in 1T-TaS$_2$, Nat. Commun. **11**, 4215 (2020).

[67] E. Martino, A. Pisoni, L. Ćirić, A. Arakcheeva, H. Berger, A. Akrap, C. Putzke, P. J. W. Moll, I. Batistić, E. Tutiš, L. Forró, and K. Semeniuk, Preferential out-of-plane conduction and quasi-one-dimensional electronic states in layered 1T-TaS$_2$, npj 2D Mater. Appl. **4**, 7 (2020).

[68] C. J. Butler, M. Yoshida, T. Hanaguri, and Y. Iwasa, Mottness versus unit-cell doubling as the driver of the insulating state in 1T-TaS$_2$, Nat. Commun. **11**, 2477 (2020).

[69] J. Lee, K.-H. Jin, and H. W. Yeom, Distinguishing a Mott insulator from a trivial insulator with atomic adsorbates, Phys. Rev. Lett. **126**, 196405 (2021).

[70] R. Bistritzer and A. H. MacDonald, Moiré bands in twisted double-layer graphene, Proc. Natl. Acad. Sci. USA **108**, 12233 (2011).

[71] O. Franke, D. Călugăru, A. Nunnenkamp, and J. Knolle, Thermal spin dynamics of Kitaev magnets: Scattering continua and magnetic field induced phases within a stochastic semiclassical approach, Phys. Rev. B **106**, 174428 (2022).

[72] A. Inbar, J. Birkbeck, J. Xiao, T. Taniguchi, K. Watanabe *et al.*, The cryogenic quantum twisting microscope, part II, Bull. Am. Phys. Soc. **68** (2023).

[73] J. Birkbeck, A. Inbar, J. Xiao, K. Watanabe, T. Taniguchi *et al.*, The cryogenic quantum twisting microscope, part I, Bull. Am. Phys. Soc. **68** (2023).

[74] G. Baskaran and P. W. Anderson, Gauge theory of high-temperature superconductors and strongly correlated Fermi systems, Phys. Rev. B **37**, 580 (1988).

[75] I. Affleck, Z. Zou, T. Hsu, and P. W. Anderson, SU(2) gauge symmetry of the large-U limit of the Hubbard model, Phys. Rev. B **38**, 745 (1988).

[76] E. Dagotto, E. Fradkin, and A. Moreo, SU(2) gauge invariance and order parameters in strongly coupled electronic systems, Phys. Rev. B **38**, 2926 (1988).

[77] X.-G. Wen and P. A. Lee, Theory of underdoped cuprates, Phys. Rev. Lett. **76**, 503 (1996).

[78] T. Senthil and M. P. A. Fisher, Z_2 gauge theory of electron fractionalization in strongly correlated systems, Phys. Rev. B **62**, 7850 (2000).

[79] P. Nozieres and D. Pines, *Theory Of Quantum Liquids*, Advanced Books Classics (Avalon, New York, 1999).

[80] Y.-D. Li, Y.-M. Lu, and G. Chen, Spinon Fermi surface $U(1)$ spin liquid in the spin-orbit-coupled triangular-lattice Mott insulator YbMgGaO$_4$, Phys. Rev. B **96**, 054445 (2017).

[81] M. Klanjšek, A. Zorko, R. Žitko, J. Mravlje, Z. Jagličić, P. K. Biswas, P. Prelovšek, D. Mihailovic, and D. Arčon, A high-temperature quantum spin liquid with polaron spins, Nat. Phys. **13**, 1130 (2017).

[82] L. Du, Y. Huang, Y. Wang, Q. Wang, R. Yang, J. Tang, M. Liao, D. Shi, Y. Shi, X. Zhou, Q. Zhang, and G. Zhang, 2D proximate quantum spin liquid state in atomic-thin α-RuCl$_3$, 2D Mater. **6**, 015014 (2018).

[83] B. Zhou, Y. Wang, G. B. Osterhoudt, P. Lampen-Kelley, D. Mandrus, R. He, K. S. Burch, and E. A. Henriksen, Possible structural transformation and enhanced magnetic fluctuations in exfoliated α-RuCl$_3$, J. Phys. Chem. Solids **128**, 291 (2019).

[84] S. Mashhadi, D. Weber, L. M. Schoop, A. Schulz, B. V. Lotsch, M. Burghard, and K. Kern, Electrical transport signature of the magnetic fluctuation-structure relation in α-RuCl$_3$ nanoflakes, Nano Lett. **18**, 3203 (2018).

[85] Y. Yu, F. Yang, X. F. Lu, Y. J. Yan, Y.-H. Cho, L. Ma, X. Niu, S. Kim, Y.-W. Son, D. Feng, S. Li, S.-W. Cheong, X. H. Chen, and Y. Zhang, Gate-tunable phase transitions in thin flakes of 1T-TaS$_2$, Nat. Nanotechnol. **10**, 270 (2015).

[86] A. W. Tsen, R. Hovden, D. Wang, Y. D. Kim, J. Okamoto, K. A. Spoth, Y. Liu, W. Lu, Y. Sun, J. C. Hone, L. F. Kourkoutis, P. Kim, and A. N. Pasupathy, Structure and control of charge density waves in two-dimensional 1T-TaS$_2$, Proc. Natl. Acad. Sci. USA **112**, 15054 (2015).

[87] M. Yoshida, Y. Zhang, J. Ye, R. Suzuki, Y. Imai, S. Kimura, A. Fujiwara, and Y. Iwasa, Controlling charge-density-wave states in nano-thick crystals of 1T-TaS$_2$, Sci. Rep. **4**, 7302 (2014).

[88] D. J. Rizzo, S. Shabani, B. S. Jessen, J. Zhang, A. S. McLeod, C. Rubio-Verdú, F. L. Ruta, M. Cothrine, J. Yan, D. G.

Mandrus, S. E. Nagler, A. Rubio, J. C. Hone, C. R. Dean, A. N. Pasupathy, and D. N. Basov, Nanometer-scale lateral p–n junctions in graphene/α-RuCl$_3$ heterostructures, Nano Lett. **22**, 1946 (2022).

[89] D. J. Rizzo, B. S. Jessen, Z. Sun, F. L. Ruta, J. Zhang, J.-Q. Yan, L. Xian, A. S. McLeod, M. E. Berkowitz, K. Watanabe, T. Taniguchi, S. E. Nagler, D. G. Mandrus, A. Rubio, M. M. Fogler, A. J. Millis, J. C. Hone, C. R. Dean, and D. N. Basov, Charge-transfer plasmon polaritons at graphene/α-RuCl$_3$ interfaces, Nano Lett. **20**, 8438 (2020).

[90] B. Zhou, J. Balgley, P. Lampen-Kelley, J.-Q. Yan, D. G. Mandrus, and E. A. Henriksen, Evidence for charge transfer and proximate magnetism in graphene–α-RuCl$_3$ heterostructures, Phys. Rev. B **100**, 165426 (2019).

[91] X. Zheng, K. Jia, J. Ren, C. Yang, X. Wu, Y. Shi, K. Tanigaki, and R.-R. Du, Tunneling spectroscopic signatures of charge doping and associated Mott transition in α-RuCl$_3$ in proximity to graphite, Phys. Rev. B **107**, 195107 (2023).

[92] A. Rossi, R. Dettori, C. Johnson, J. Balgley, J. C. Thomas, L. Francaviglia, A. K. Schmid, K. Watanabe, T. Taniguchi, M. Cothrine, D. G. Mandrus, C. Jozwiak, A. Bostwick, E. A. Henriksen, A. Weber-Bargioni, and E. Rotenberg, Direct visualization of the charge transfer in graphene/α-RuCl$_3$ heterostructure, Nano Lett. **23**, 8000 (2023).

[93] M. A. Altvater, S.-H. Hung, N. Tilak, C.-J. Won, G. Li, S.-W. Cheong, C.-H. Chung, H.-T. Jeng, and E. Y. Andrei, Revealing the charge density wave proximity effect in graphene on 1T-TaS$_2$, arXiv:2201.09195.

[94] C. Boix-Constant, S. Mañas-Valero, R. Córdoba, J. Baldoví, Á. Rubio, and E. Coronado, Out-of-plane transport of 1T-TaS$_2$/graphene-based van der Waals heterostructures, ACS Nano **15**, 11898 (2021).

[95] M. A. Altvater, N. Tilak, S. Rao, G. Li, C.-J. Won, S.-W. Cheong, and E. Y. Andrei, Charge density wave vortex lattice observed in graphene-passivated 1T-TaS$_2$ by ambient scanning tunneling microscopy, Nano Lett. **21**, 6132 (2021).

[96] R. Zhao, Y. Wang, D. Deng, X. Luo, W. J. Lu, Y.-P. Sun, Z.-K. Liu, L.-Q. Chen, and J. Robinson, Tuning phase transitions in 1T-TaS$_2$ via the substrate, Nano Lett. **17**, 3471 (2017).

[97] M. Agarwal and E. G. Mishchenko, Dynamic response functions of two-dimensional Dirac fermions with screened Coulomb and short-range interactions, Phys. Rev. B **102**, 125421 (2020).